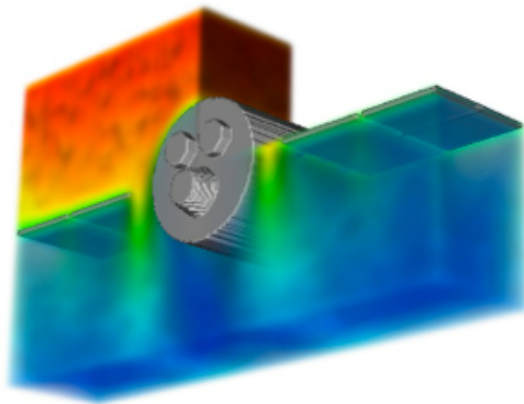


AFOSR Research Grant FA9550-15-1-0407

Faster-than-Realtime Electrostatic Force and Torque Modeling for SSA Applications

(2016 Annual Report)



Principal Investigators:

Hanspeter Schaub¹ (PI)
University of Colorado, Boulder, CO 80309-0431

September 14, 2016

¹Alfred T. and Betty E. Look Professor of Engineering, hanspeter.schaub@colorado.edu, (303) 492-2767

Table of Contents

1	Technical Progress Reports	2
1.1	Research Thrust 1: MSM Development	2
1.1.1	Volume-MSM Setup Optimization	3
1.1.1.1	E-Field Truth Models in Maxwell 3D	4
1.1.1.2	Investigate Robust VMSM Sphere Optimization	6
1.1.1.2.1	Optimization Self Capacitance Constraints	6
1.1.1.2.2	Example Optimization Case	8
1.1.1.2.2.1	2-Sphere Self-Capacitance	8
1.1.1.2.2.2	3-Sphere Self-Capacitance	9
1.1.1.2.3	Matrix Inversion	10
1.1.1.2.3.1	2-Sphere Case	11
1.1.1.2.3.2	3-Sphere Case	11
1.1.1.2.4	Optimization Results	11
1.1.1.2.4.1	3-Sphere, 3-MSM Parameters Model	13
1.1.1.2.4.2	3-Sphere, 2-MSM Parameters Model	13
1.1.1.2.4.3	2-Sphere 2-MSM Parameters Model	14
1.1.1.2.4.4	2-Sphere 1-MSM Parameter Model	15
1.1.1.2.4.5	2-Sphere Cost Functions	15
1.1.1.2.4.6	Summary of Cases	16
1.1.1.2.5	Far-Field Probe Radii Conditioning	18
1.1.1.2.6	E-Field Matching	18
1.1.1.3	Validate MSM on Multiple Shapes	18
1.1.1.3.1	Fitting VMSM to a Star Wars Tie-Fighter	19
1.1.1.3.2	Fitting VMSM to a Box-Panel Spacecraft	20
1.1.1.3.2.1	VMSM Model from Maxwell3D FEA data	20
1.1.1.3.2.2	VMSM Model from High-Fidelity SMSM data	24
1.1.2	Surface-MSM Setup Optimization	28
1.1.3	Comparison to Appropriate Fidelity Models (AFMs)	30
1.1.3.1	Development of Appropriate Fidelity Models (AFMs)	30
1.1.3.1.1	Force Derivation	31
1.1.3.1.2	Torque derivation	34
1.1.3.2	Radial Field	35
1.1.3.3	Flat Field	35
1.1.3.3.1	Force Derivation:	36
1.1.3.3.2	Torque Derivation:	37
1.1.3.3.3	MSM and AFM equivalency in flat fields	37
1.1.3.4	Predictive AFMs	38

1.1.3.4.1	Inter-Craft predictive AFMs	38
1.1.3.4.1.1	Susceptibility of the Scalar Charge	40
1.1.3.4.1.2	Susceptibility of the Dipole	40
1.1.3.4.1.3	Susceptibility of the Charge Tensor	41
1.1.3.4.2	Flat Field Susceptibilities	41
1.1.3.5	Inter-Craft Analysis	42
1.1.3.6	Flat field Analysis	43
1.1.3.6.1	Eddy Current Torque	44
1.1.3.6.2	Analytical Bounding Cases	44
1.1.3.6.3	Numerical Analysis of Orbit	45
1.1.3.6.3.1	Self Capacitance Estimation	46
1.1.3.6.3.2	AFM parameter estimation through SMSM	46
1.1.3.6.3.3	Magnetic Field and Charging Models	47
1.1.3.6.3.4	Nominal Numerical Propagation	48
1.1.3.6.4	Trade studies	50
1.1.3.6.4.1	Plate Area and Aspect Ratio	50
1.1.3.6.4.2	Initial attitude	51
1.1.3.6.4.3	Initial Spin Rate	52
1.1.3.6.5	Flat Field Analysis Summary	52
1.2	Research Thrust 2: Flexible Shape MSM Applications	52
1.2.1	Study Flexible Wire Shapes	53
1.2.2	Experiments on Wires	53
1.2.2.1	Atmospheric Experiments	53
1.2.2.2	Vacuum Chamber	56
1.2.3	Conclusions and Future Work	58
1.3	Research Thrust 3: Dielectric Surfaces	58
1.3.1	Study Time Dependent Dielectric Charging	58
1.3.2	Consider space dielectric charging (Nascap-2K)	61
1.3.3	Expand MSM model to incorporate insulators	61
2	Conclusions and Planned Work	63
2.1	Conclusions	63
2.2	Year 2 Planned Work	63
	Bibliography	66

Chapter 1

Technical Progress Reports

This chapter discusses the technical results achieved over the last project year. The sections and sub-sections are numbered to match the research thrusts and tasks outlined in the GANTT chart in Figure ??.

1.1 Research Thrust 1: MSM Development

One way to calculate the electrostatic forces and torques on a spacecraft is to use a commercial FEA tool, such as ANSYS's Maxwell 3D. However, even with relatively low accuracies, these tools usually require on the order of minutes to complete analyses of simple two-body systems, which is unsuitable for modeling dynamics in real-time for state estimation or control applications.

By reducing the spacecraft geometry to a collection of charged spheres, the configuration of which are dependent on the geometry and conductivity of the spacecraft being modeled, MSM can approximate electrostatic forces and torques several orders of magnitude more quickly than commercial FEA tools with minimal decrease in the resulting accuracy.

As shown in Figure 1.1, MSM approximates a spacecraft as a collection of spheres with variable positions and radii. The voltage on any sphere is a function of both its own charge and the charge of nearby spheres. If these spheres are far enough away to be approximated as point charges, the voltage is given by:³

$$V_i = \frac{1}{4\pi\epsilon_0} \frac{q_i}{R_i} + \sum_{j=1, j \neq i}^m \frac{1}{4\pi\epsilon_0} \frac{q_j}{\rho_{i,j}} \quad (1.1)$$

Where q_i and R_i are the charge and radius of the i^{th} sphere, respectively, $\rho_{i,j}$ is the center-to-center distance between spheres i and j , and ϵ_0 is the permittivity of free space constant. If the voltages of each sphere are given by $\mathbf{V} = [V_1, V_2, \dots, V_m]^T$ and the charges are given by $\mathbf{q} = [q_1, q_2, \dots, q_m]^T$, the relationship between the two is

$$\mathbf{V} = [\mathbf{C}]^{-1} \mathbf{q} \quad (1.2)$$

where $[\mathbf{C}]$ is the Position Dependent Capacitance (PDC) matrix whose inverse is defined below:³

$$\mathbf{V} = [\mathbf{C}]^{-1} \mathbf{q} = \frac{1}{4\pi\epsilon_0} \begin{bmatrix} 1/R_1 & 1/\rho_{1,2} & \cdots & 1/\rho_{1,m} \\ 1/\rho_{2,1} & 1/R_2 & \cdots & 1/\rho_{2,m} \\ \vdots & \vdots & \ddots & \vdots \\ 1/\rho_{m,1} & 1/\rho_{m,2} & \cdots & 1/R_m \end{bmatrix} \begin{bmatrix} q_1 \\ q_2 \\ \vdots \\ q_m \end{bmatrix} \quad (1.3)$$

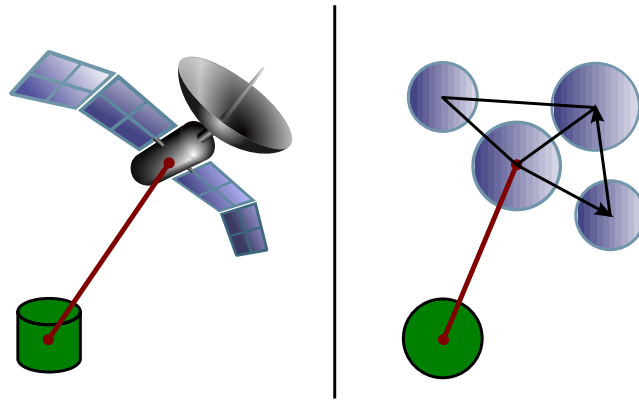


Figure 1.1: Approximation of a satellite as a collection of charged spheres.³

The voltage on each sphere can be determined as a function of various factors, such as photo-electron current resulting from UV radiation and interactions with the plasma environment.^{4,5} For purposes of this paper, the charged bodies are assumed to be perfect conductors. Thus, the voltage of each sphere for a given body is the same ($V_i = V_j$) and is equal to the voltage of the body. The PDC matrix can be inverted to obtain the charge on each sphere. Once the charges on each sphere are known, the forces and torques can be computed as shown in Eqs. (1.4) and (1.5). An origin O at the center of mass of the body is used for \mathbf{r}_i ; the force and torque calculated about this origin are

$$\mathbf{F} = -k_c q_B \sum_{i=1}^n \frac{q_i}{r_{i,b}^3} \mathbf{r}_{i,b} \quad (1.4)$$

$$\mathbf{L}_O = -k_c q_B \sum_{i=1}^n \frac{q_i}{r_{i,b}^3} \mathbf{r}_i \times \mathbf{r}_{i,b} \quad (1.5)$$

With minimal loss of accuracy — of a few percent or less — MSM is a promising way to solve for the electrostatic forces and torque on a spacecraft faster than real-time. However, it relies on knowledge of the position and size of all spheres in the model, which in previous work have been laboriously hand tuned.^{3,6} This paper seeks to develop an automated means of determining the position and size of these spheres, such that the force and torque calculated from the model match closely with the data provided by a commercial electrostatic FEA tool.

1.1.1 Volume-MSM Setup Optimization

An optimal MSM sphere distribution can be obtained by employing optimization techniques, whereby the desired sphere distribution minimizes the force and torque prediction error. Optimizing the sphere distribution uses the size and body-fixed location of each MSM sphere included in the model as state variables. For this analysis, MATLAB's built-in *fmincon* optimizer is used.

Optimization problems are driven by a cost function. Two cost functions were implemented and compared in this study. The first cost function J_{rel} , based on the relative difference between VMSM and Maxwell forces and torques, is defined as:

$$J_{\text{rel}} = f_{\text{rel}} + t_{\text{rel}} \quad (1.6)$$

$$f_{\text{rel}} = \sum_{i=1}^n \frac{\|\mathbf{F}_{\text{VMSM}_i} - \mathbf{F}_{\text{Maxwell}_i}\|}{\|\mathbf{F}_{\text{Maxwell}_i}\|} \quad (1.7)$$

$$t_{\text{rel}} = \sum_{i=1}^n \frac{\|\mathbf{T}_{\text{VMSM}_i} - \mathbf{T}_{\text{Maxwell}_i}\|}{\|\mathbf{T}_{\text{Maxwell}_i}\|} \quad (1.8)$$

Where $\mathbf{F}_{\text{VMSM}_i}$ denotes the predicted force vector at the i^{th} comparison point, $\mathbf{F}_{\text{Maxwell}_i}$ is the truth model force vector evaluated at that same comparison point, and similar definitions are made for torque. One drawback of using relative differences in a cost function is the potential for small absolute differences to result in large relative differences. This is very likely to happen in the far field when the force and torque in the truth model are very small.

Consequently, the second cost function J_{abs} is based on the absolute difference between VMSM and Maxwell forces and torques:

$$J_{\text{abs}} = f_{\text{abs}} + t_{\text{abs}} \quad (1.9)$$

$$f_{\text{abs}} = \frac{\sum_{i=1}^n \|\mathbf{F}_{\text{VMSM}_i} - \mathbf{F}_{\text{Maxwell}_i}\|}{\sum_{i=1}^n \|\mathbf{F}_{\text{Maxwell}_i}\|} \quad (1.10)$$

$$t_{\text{abs}} = \frac{\sum_{i=1}^n \|\mathbf{T}_{\text{VMSM}_i} - \mathbf{T}_{\text{Maxwell}_i}\|}{\sum_{i=1}^n \|\mathbf{T}_{\text{Maxwell}_i}\|} \quad (1.11)$$

By distributing the sum into the denominator, errors that occur when the FEA solution is small are not heavily weighted. This is advantageous because when the FEA force and torque are small, there is often a lot of noise in the solution.

To easily assess the quality of the solution, Eqs. (1.7) and (1.8), which are analogous to relative error, can be used. Since f_{rel} and t_{rel} are cumulative quantities, their averages will provide a relative error representative of the quality of a given solution. This relative error can be multiplied by 100 to obtain a percentage error measure that is used to quantify the quality of a particular geometric solution determined by optimization during this analysis.

1.1.1.1 E-Field Truth Models in Maxwell 3D

The cost functions feeds back on the difference between VMSM and Maxwell. Ansys Maxwell 3D is a very powerful commercial Finite Element Analysis tool which is capable of solving low frequency and electrostatic problems. In this electrostatic application, the poisson equation

$$\nabla^2 V = \frac{\rho}{\epsilon} \quad (1.12)$$

is solved across the entire region. Once the charge distribution is known, the force and torque on a object in the region is found and used at truth.

Maxwell requires geometry, materials, and excitations to be set before solving. The geometry consists of the dimensions and positions of all objects in the region. Each object in the region must be assigned to be a conductor or dielectric. Many common dielectrics are listed, but in this analysis most materials are assigned to be “perfect conductors” with a resistivity of 0. Lastly the excitations must be set. The most common excitation for this analysis was voltage. For instance to

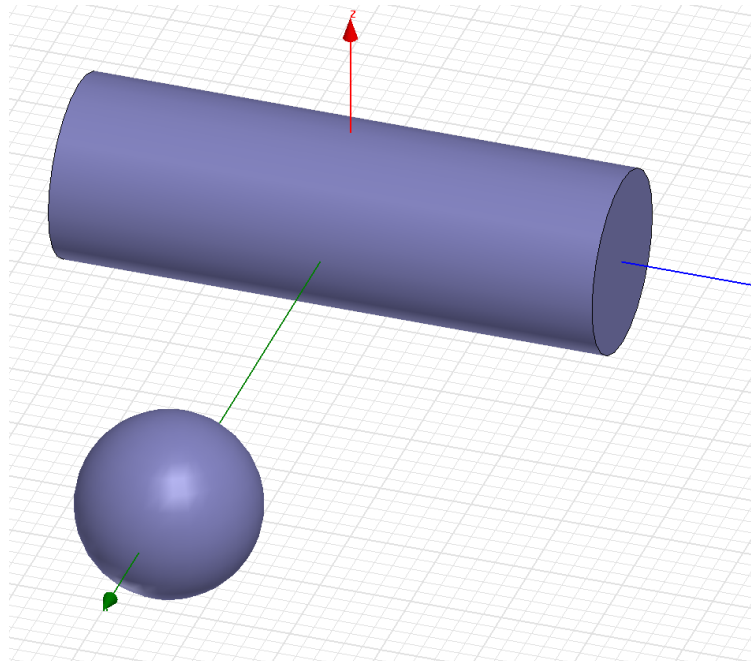


Figure 1.2: Example Maxwell setup

compute the force and torque between a sphere and cylinder, the sphere might be set to +30 kV, and the cylinder might be set to -30 kV. The voltage on a virtual box with a uniform axis offset of 1000% must be set to 0 V in order to get sensible answers.

Although Maxwell is a very powerful commercial FEA software package, there are some problems that cause it to give counter-intuitive answers. For example, when one object is much smaller than another, and they are very far apart, the deviation from the first order solution $F = \frac{q_1 q_2 r}{4\pi\epsilon_0 r^3}$ is in the hundreds of percent. While induced effects can make a large difference when the objects are large compared to their separation, the deviations from the point force solution are expected to be minimal when they are far away. The reason for this may be a lack of grid refinement when one object is much smaller in size than the other.

Additionally, when two similarly sized objects are far apart (~ 10 times their diameter), the torques on either object are not smooth functions of position. When objects have very complex geometries, especially convex ones, it is intuitive for the torque on one object to be a non-smooth function of the position of the other object. However, with our cylinder-sphere system, the torque on the cylinder seems overly noisy when the sphere sweeps our a clean arc. This might also be caused by a lack of grid refinement.

Maxwell does give good results for two similarly sized objects that are close relative to their size. To get forces in the far field, a variable-sized probe is used. As the probe moves farther away from the test object, it now gets larger. Because of its larger size it has a larger self capacitance and therefore more charge if the voltage is held constant. This increases the force as well. A trade study was conducted to the relationship between the distance between the probe and test object and the probe's radius that minimized the difference between Maxwell's force computation and the point force formula. This formula should be close to the true answer when the objects are far apart.

Another option to remove the unintuitive results is to augment Maxwell's data with data provided by a Surface MSM (SMSM) model. In this model, large numbers (~ 100) of spheres are placed uniformly across the surface of an object such as a cylinder, sphere, or cube. All spheres have

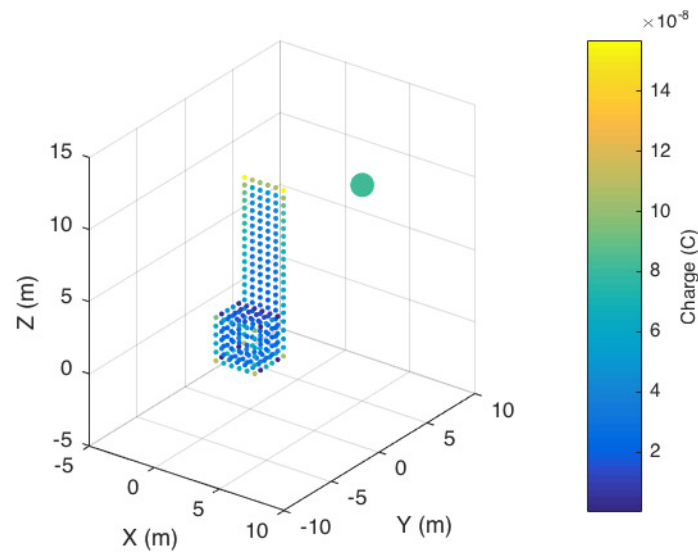


Figure 1.3: Example of SMSM truth model

the same radius, which is set so that self capacitance of the SMSM model is equal to the self capacitance of the actual object, which can be found through Maxwell. SMSM has been shown in Reference 6 to have good agreement with Maxwell in the near field where it gives more trustworthy results, and additionally gives smooth results in the far field. The use of SMSM models to develop high-fidelity smooth fitting data for VMSM models is discussed later on in section 1.1.2.

1.1.1.2 Investigate Robust VMSM Sphere Optimization

There are many considerations when optimizing a VMSM model. Constraints can be used to limit the search space and enforce physical behavior in the far field for instance. This is investigated for the example case of a cylinder and sphere. Future work will expand this concept for more constraints and more general shapes.

1.1.1.2.1 Optimization Self Capacitance Constraints

There are a number of fundamental vectors and matrices that are constant for a given shape and are derived in the AFM section 1.1.3. At present the only constraint being used is self capacitance. Previous work with MSM focused on matching forces and torques between two charged objects separated by less than ten craft radii without regard to matching the self capacitance of the objects.³ An MSM geometry determined under these conditions will generally perform well at these distances, but will suffer from significant errors at larger distances. As the separation distance between the two objects grows large, the objects will effectively become as isolated point spheres. At this point, the total charge of each object is approximated with Eq. (1.13), which only requires knowledge of the self-capacitance. If the MSM parameters do not yield a self-capacitance C which matches the self-capacitance of the actual shape, then the electrostatic force predictions are ensured to be incorrect at large separation distances.

The proposed MSM optimization method constrains the self capacitance calculated using Eq. (1.16) to be equal to the self capacitance found using an commercial electrostatic FEA tool. The three primary benefits for using this constraint are:

- The MSM solution will automatically provide accurate results at large distances.

By enforcing fundamental physics, predicting forces in the far field will always give good results, while still allowing the subtlety needed to model the complex interactions in the near field.

- The MSM optimization will no longer be swayed by noisy data in the far field.

Generating or measuring truth forces and torques becomes increasingly noisy as the separation distance between charged objects increases. Fitting the MSM parameters to match such noisy data can pose significant challenges to numerical optimization algorithms and can reduce the accuracy of the solution. Instead, by constraining the MSM parameters to satisfy the known self-capacitance of a shape, the lower quality electrostatic force and torque solutions at larger separation distances can be ignored.

- Enforcing the self capacitance constraint eliminates one degree of freedom.

By reducing the MSM parameter search space, the computational time for the optimization process is reduced. It goes without saying that this is desirable in the automation of sphere geometry. However, this reduced computational time can come at the cost of slightly decreased accuracy in cases where separation distances is small.

The self capacitance constraint can be enforced either numerically or analytically. An analytical constraint is always more accurate than a numerical constraint. However, an analytical constraint may not always be available. Forming the self capacitance requires inverting an $N \times N$ matrix and summing all the elements, where N is the number of spheres in the MSM model. This can become difficult for cases involving a large number of spheres.

The self capacitance can be formed from a MSM model by dividing the total charge by the voltage.

$$C = \frac{Q}{V} \quad (1.13)$$

The total charge is given by

$$Q = \sum_{i=1}^N q_i \quad (1.14)$$

Using Eq. (1.13) the charge vector is written as

$$q_i = \sum_{j=1}^N C_{ij} V_j \quad (1.15)$$

Recalling that the voltage on each sphere within the object is assumed to be the same ($V_j = V$), substituting Eqs. (1.14) and (1.15) into Eq. (1.13) yields

$$C = \frac{Q}{V} = \frac{\sum_{i=1}^N \sum_{j=1}^N C_{ij} V_j}{V} = \sum_{i=1}^N \sum_{j=1}^N C_{ij} \quad (1.16)$$

The total capacitance C of an MSM model is the sum of the individual elements of the PDC matrix $[C]$. Recall that $[C]$ is obtained by inverting $[C]^{-1}$, defined in Eq. (1.3).

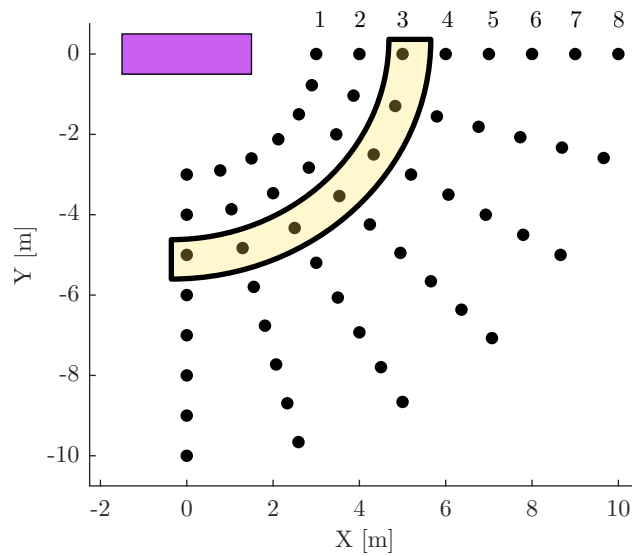


Figure 1.4: Geometric Parameters for Maxwell Force and Torque Calculations

1.1.1.2.2 Example Optimization Case

A convenient system to model is a cylinder, representing a defunct rocket body upper stage, and a sphere, representing a controlled and charged space tug. The cylinder has a length of three meters and a diameter of one meter, and the sphere has a diameter of one meter. In Reference 3 the cylinder is approximated using three collinear spheres, as shown in Figure 1.6, with the end spheres set at an equal distance away from the center sphere. The cylinder models with either two or three collinear spheres are considered in the scope of this paper.

Both the cylinder and the sphere are held at +30,000 Volts. Forces and torques are calculated at multiple points as shown in Figure 1.4. The points are distributed cylindrically, with radius changing by one meter and angle changing by 15° between each point. These points can be grouped by their distance from the cylinder; each set of equidistant points is referred to as a *ring* and are labeled in Figure 1.4.

The points included in the rings at larger distances will have smaller forces that are either negligible or describable by approximating the cylinder with a single sphere. It may be unnecessary to include these rings in the optimization process, particularly if solution quality is not reduced. Thus, this analysis will also examine the effects of these rings on solution quality and computational time.

1.1.1.2.2.1 2-Sphere Self-Capacitance

Consider a cylinder modeled by 2 collinear spheres of equal radius, as shown in Figure 1.5. The model is described by two independent variables: the radii of each sphere r and the distance between the two spheres ρ .

Eq. (1.16) is used to express the self capacitance of the two sphere system as

$$C = 4\pi\epsilon_0 \frac{2r\rho}{\rho + r} \quad (1.17)$$

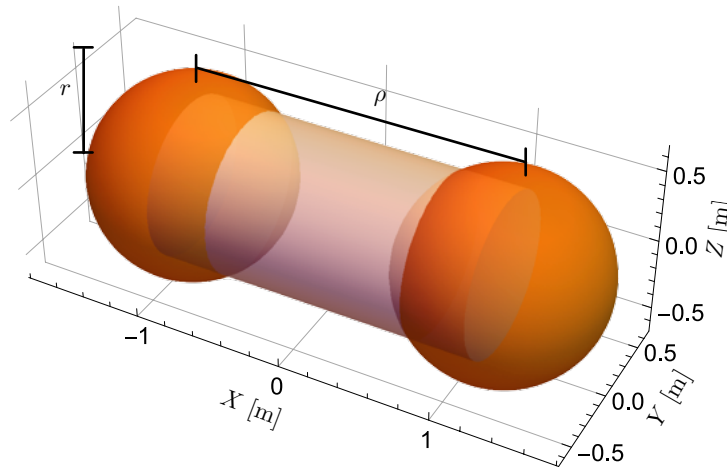


Figure 1.5: Two Sphere MSM Model of a Cylinder

The independent variables r and ρ are expressed individually as

$$r = \frac{\rho C_{\text{mod}}}{2\rho - C_{\text{mod}}} \quad (1.18)$$

$$\rho = \frac{r C_{\text{mod}}}{2r - C_{\text{mod}}} \quad (1.19)$$

where C_{mod} is the scaled self capacitance

$$C_{\text{mod}} = \frac{C}{4\pi\epsilon_0} \quad (1.20)$$

Eq. (1.18) is used to write r as a function of ρ or vice versa with Eq. (1.19). Thus, there is only one independent variable in this two sphere MSM case.

1.1.1.2.2.2 3-Sphere Self-Capacitance

Next, a cylinder is modeled by 3 collinear spheres, as shown in Figure 1.6. In this case, the identically sized end spheres are equidistant from the center sphere, which has a different radius. Three independent variables exist in this scenario: the radii of the end sphere r , the radius of the center sphere R , and the distance between the center sphere and the end sphere ρ .

As with the 2 sphere model, there are analytic results for the self capacitance of the sphere in terms of the axially constrained MSM sphere placement and size parameters. The self capacitance is

$$C = 4\pi\epsilon_0 \frac{\rho(-7rR + 2\rho(2r + R))}{\rho(2\rho + r) - 4rR} \quad (1.21)$$

Direct substitution yields a reduced set of unknown MSM parameters and allows the 3 MSM parameters to be expressed in terms of the other 2 and the true self capacitance using:

$$r = \frac{2\rho^2(R - C_{\text{mod}})}{C_{\text{mod}}\rho - 4C_{\text{mod}}R + 7R\rho - 4\rho^2} \quad (1.22)$$

$$R = \frac{\rho(4r - 2C_{\text{mod}}\rho - C_{\text{mod}}r)}{7r\rho - 2\rho^2 - 4C_{\text{mod}}r} \quad (1.23)$$

$$\rho = \frac{-(C_{\text{mod}}r + 7rR) \pm \sqrt{(C_{\text{mod}}r + 7rR)^2 + 4(2C_{\text{mod}} - 4r + 2R)(4C_{\text{mod}}Rr)}}{2(2C_{\text{mod}} - 4r + 2R)} \quad (1.24)$$

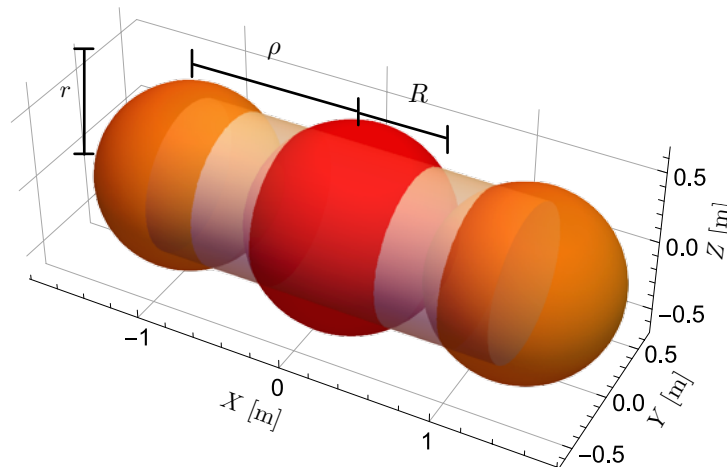


Figure 1.6: Three Sphere MSM Model of a Cylinder

This allows the numerical optimizer to search only 2 parameters instead of the original 3. If only the set of three parameters (R, r, ρ) are considered that satisfy the MSM self capacitance equality constraint, all admissible MSM parameters must lie on a two-dimensional surface, as shown in Figure 1.7.

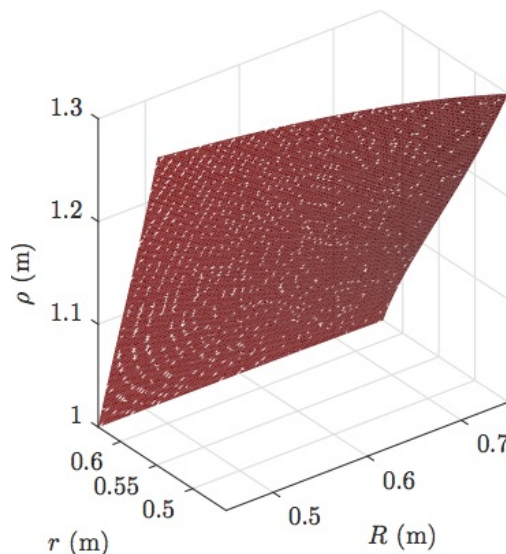


Figure 1.7: Isosurface Showing Where the Cylinder Self-Capacitance is 106.8345 pF

Although analytical constraints exist for the restricted 2-sphere and 3-sphere MSM cases, such a simple solution may not always exist. In the general case of N spheres, a numerical constraint must be enforced.

1.1.1.2.3 Matrix Inversion

Certain sets of MSM parameters can make the inverse of the PDC difficult or impossible to invert, which yields non-physical results such as negative or infinite self capacitance. To avoid these singularities, the determinant can be analytically constrained to be non-zero, which yields relationships between MSM parameters to be avoided. This is done for the 2- and 3-sphere cases

considered in this paper.

1.1.1.2.3.1 2-Sphere Case

For two collinear spheres of equal radius, the inverse of the PDC is given by

$$[C]^{-1} = \frac{1}{4\pi\epsilon_0} \begin{bmatrix} \frac{1}{R} & \frac{1}{\rho} \\ \frac{1}{\rho} & \frac{1}{R} \end{bmatrix} \quad (1.25)$$

Where R is the sphere radius and ρ is their separation. The determinant of this matrix is

$$\det([C]) = \frac{1}{R^2} - \frac{1}{\rho^2}$$

By ensuring $R \neq \rho$ the matrix is invertible and MSM provides valid results. In addition, as $R \rightarrow \rho$ the matrix becomes numerically ill-conditioned.

1.1.1.2.3.2 3-Sphere Case

For three collinear spheres, where the outer spheres are constrained to be the same size but the center sphere radius is free, the matrix is somewhat more complicated. The inverse of the capacitance matrix is now given by

$$[C]^{-1} = \frac{1}{4\pi\epsilon_0} \begin{bmatrix} \frac{1}{r} & \frac{1}{\rho} & \frac{1}{2\rho} \\ \frac{1}{\rho} & \frac{1}{R} & \frac{1}{\rho} \\ \frac{1}{2\rho} & \frac{1}{\rho} & \frac{1}{r} \end{bmatrix} \quad (1.26)$$

Where r is the end sphere radius, R is the center sphere radius, and ρ is the distance from the center of the end sphere to the center of the center sphere. The determinant is now

$$\det([C]) = \frac{(2\rho - r)(2\rho^2 + r\rho - 4rR)}{4\rho^3 r^2 R} \quad (1.27)$$

This determinant has two roots: $2\rho - r = 0$ and $2\rho^2 + r\rho - 4rR = 0$. The first one is easily visualized as the end radius being twice the distance to the center. This means that the edge of the leftmost sphere touches the center of the rightmost sphere. The parameter sets of both roots are illustrated in Figure 1.8.

These surfaces in the 3-dimensional parameter space must be avoided to ensure model validity. This does not reduce the degrees of freedom, but does require parameter checking.

1.1.1.2.4 Optimization Results

The goal of this study is to automate the process of distributing MSM spheres through the volume of a body to best match the force and torque experienced by that body when in the presence of a second craft. The automation process uses an optimization routine to move the center position and set the radius of each MSM sphere. The optimization state therefore becomes the set of

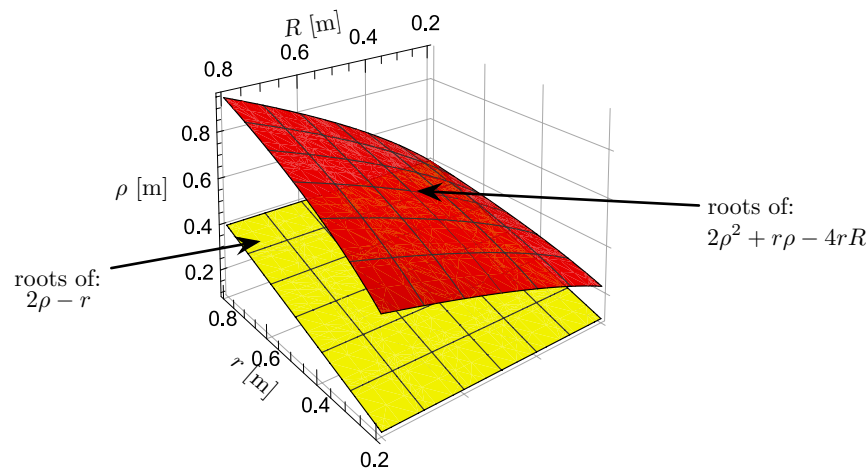


Figure 1.8: Surfaces where the determinant of the PDC Matrix is zero

Table 1.1: Baseline Geometric Parameters

	Sphere 1	Sphere 2	Sphere 3
X Coordinate (m)	0	0	0
Y Coordinate (m)	-1.1454	0	1.1454
Z Coordinate (m)	0	0	0
Radius (m)	0.5959	0.6534	0.5959

geometrical parameters that describe the locations and sizes of all MSM spheres in the body. The baseline to which new geometric parameters are compared are the numbers in Table 1.1, which are presented in Reference 3. The coordinates and sphere definitions in Table 1.1 are based on the geometry of Figure 1.6.

The baseline geometric parameters can be expressed in the three parameter set as

$$R = 0.6534$$

$$r = 0.5959$$

$$\rho = 1.1454$$

These parameters generate a solution with a relative force error of 1.47% and a relative torque error of 1.18%.

The initial conditions for the optimization create spheres of equal radii that have surface area equal to the cylinder model. Under these conditions, the optimization produces solutions with relative errors ranging from 1.1% to 3.9% for force and 0.1% to 4.1% for torque, depending on the number of data-point rings used in the optimization, the inclusion of the capacitance constraint, and the cost function used. Generally speaking, the solutions provided by this optimizer approach are comparable to the accuracy previously achieved with the significant benefit that all solutions are generated in less than ten seconds — orders of magnitude faster than the thousands of seconds previously required.⁶

Four cases are examined in further detail to demonstrate the flexibility of the algorithm and the current challenges in automating sphere placement: a three sphere cylinder model with and without the previously described capacitance constraint and a two sphere cylinder model with and without the previously described capacitance constraint. Each case is analyzed with the relative

and absolute difference cost functions, as described by Eqs. (1.6) and (1.9). The best results of all eight cases are tabulated in Table 1.2.

1.1.1.2.4.1 3-Sphere, 3-MSM Parameters Model

The first case uses three spheres to model the cylinder and does not use a capacitance constraint, as shown in Figure 1.6. The initial conditions chosen for the optimization are $r = R = 0.54$ meters and $\rho = 1.5$ meters.

Figure 1.9 plots the relative force and torque error and computational time against the number of rings used in the optimization. It should be noted that, even if less than eight rings were used for the optimization, the relative error is calculated by comparing the solution against all possible data points in the eight rings. As expected, including more data in the optimization improves the prediction over the data range considered. An important aspect of this trend is how both the force and torque error begin to level out when more than three rings are included. This indicates that data from outer rings could be ignored, especially since computational times increase with increased data.

The relative difference and absolute difference cost functions complete the optimization in about the same amount of time. However, the relative difference cost function shows significantly lower error in force and torque as the number of rings used in the optimization increases. Particularly notable is the near-zero torque error when seven or eight rings of data are used. Because of this, it can be concluded that the relative difference cost function is much better at matching data than the absolute difference cost function.

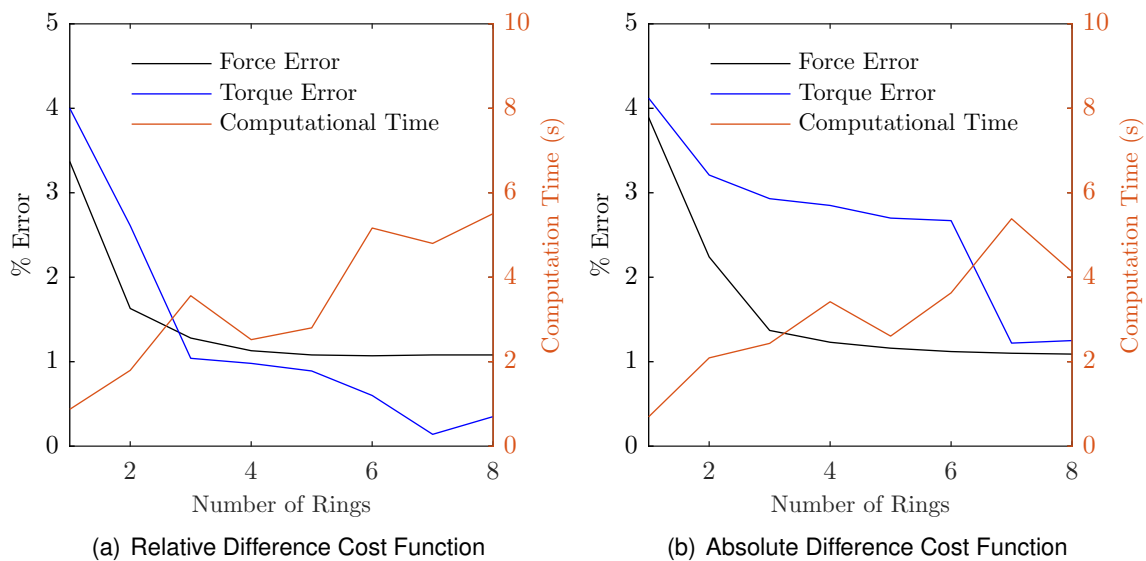


Figure 1.9: Three Sphere VMSM Performance, Without Capacitance Constraint

1.1.1.2.4.2 3-Sphere, 2-MSM Parameters Model

The second case uses the same three sphere setup as the first, but adds an analytical capacitance constraint as described by Eqs. (1.22) through (1.24). In this case, the constraint for the end radius r , is implemented, leaving the center radius R and the separation distance ρ as the independent variables.

In Figure 1.10, the relative force and torque error and computational time are plotted against the number of rings used in the optimization. Of note of the error trends under the capacitance constraint is the force error, which remains constant regardless of the number of rings used. This is due to the nature of the capacitance constraint, which causes the VMSM model to resemble a single point charge at large distances. At large distances, all that is needed to model force is the capacitance of the object.⁶ While matching capacitance can model force with a high degree of accuracy, it cannot model torque quite as well because of induced charging effects on the cylinder.

With the exception of using seven or eight rings under the absolute difference cost function, the 2 Parameter Model completes the optimization more quickly than the 3 Parameter Model. This supports the assumption that reducing the parameter search space would decrease the computation time. Since both the 3 Parameter Model and 2 Parameter Model result in similar errors, it may be more useful to use the 2 Parameter Model for optimizations on account of its speed.

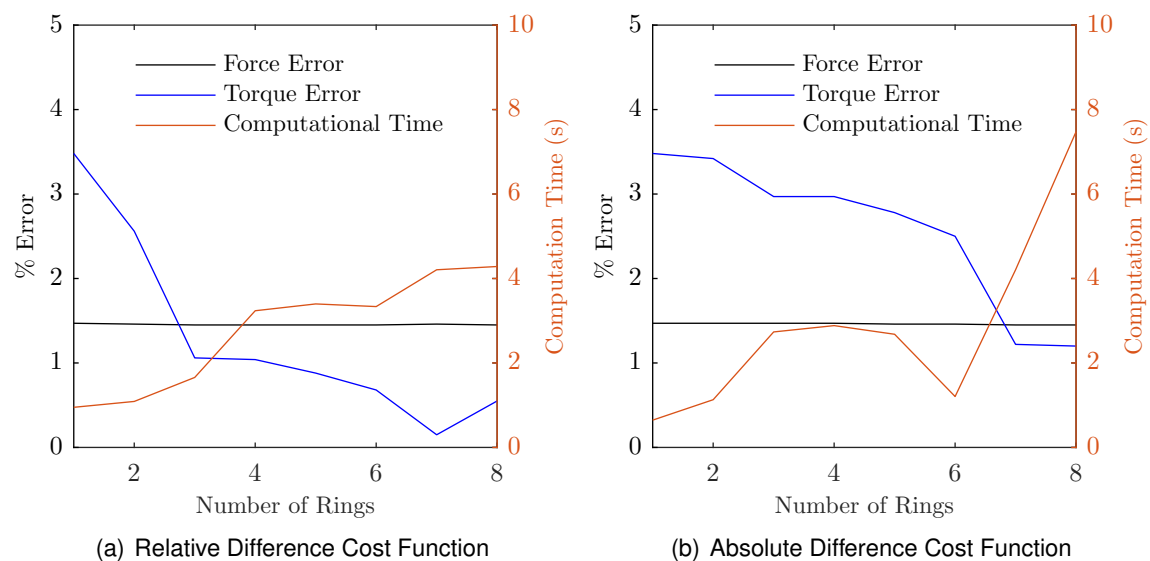


Figure 1.10: Three Sphere VMSM Performance, With Capacitance Constraint

1.1.1.2.4.3 2-Sphere 2-MSM Parameters Model

The third case uses a two sphere model for the cylinder, as shown in Figure 1.5, without the capacitance constraint. The initial conditions chosen are $r = 0.6614$ meters and $\rho = 1.5$ meters. Because there are only two independent variables (r and ρ), the optimization in this case should run much faster than that for the unconstrained three sphere model. This is observed in Figure 1.11, where computational time for determining the solution is under two seconds for most ring and cost function combinations. In contrast, many of the three sphere cases, even if constrained by capacitance to use two parameters, took more than three seconds to find a solution.

As with the three sphere models, the errors on the two sphere model, particularly for force, begin to level off after three rings of data are used; this is especially apparent for the absolute difference cost function. This trend indicates that not all rings are necessary to produce a solution that can reasonably match a truth model. The relative difference cost function also provides lower errors in torque than the absolute difference cost function, suggesting again that the relative difference cost function is better suited for these optimizations.

The errors in the two sphere model are on the same order of magnitude as for the three sphere model, while the optimization takes about half the time to run. This suggests that it may be more practical to use the two sphere model in some cases, particularly where computational time is of importance.

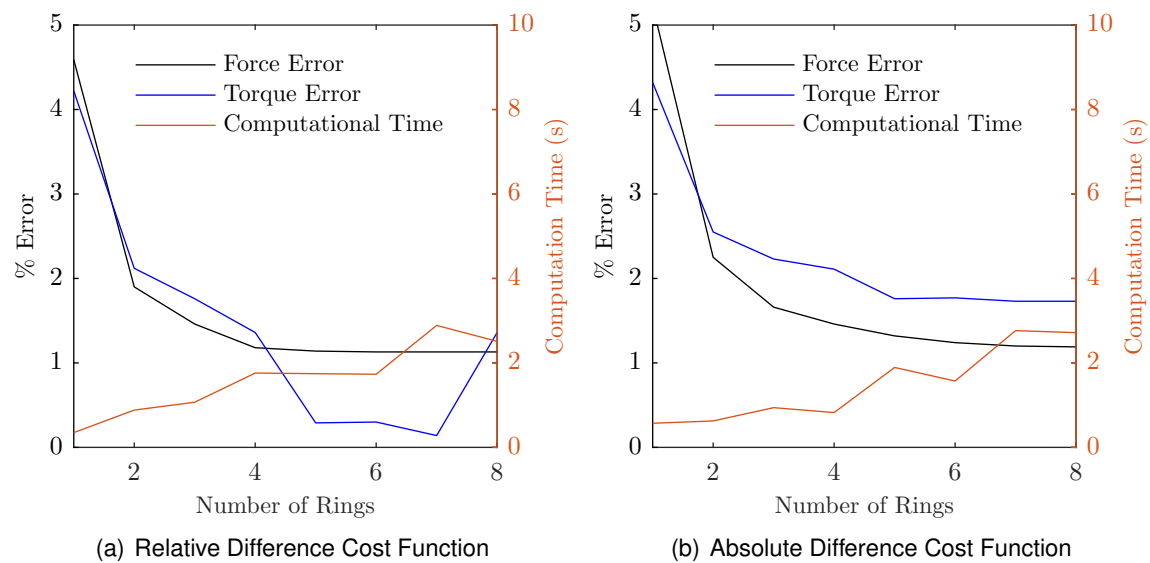


Figure 1.11: Two Sphere VMSM Performance, Without Capacitance Constraint

1.1.1.2.4.4 2-Sphere 1-MSM Parameter Model

The fourth case uses a two sphere model for the cylinder while enforcing a capacitance constraint. By using Eq. (1.24) to constrain the optimization to one independent variable r , the computational time should decrease while having minimal effects on the errors. Figure 1.12 shows the error and computational time plots.

As with the capacitance constrained three sphere model (Figure 1.10), the force errors in this case are constant regardless of the number of rings used for the optimization. While it was expected that the capacitance constraint would allow force to be accurately accounted for at large distance, the constant errors provided by the solution were not. It appears that the capacitance of the model, rather than the geometric sphere configuration, is key to accurately determining forces acting on a charged object.

While capacitance cannot provide the same accuracy for torque calculations, it is still notable that errors change very little after five rings of data are included — even dropping below 1% error. It should be noted that such low error values may very well result from overfitting a solution to noisy data; however, the low errors demonstrate that it is possible to obtain close matches to truth data without using all the rings available.

1.1.1.2.4.5 2-Sphere Cost Functions

It is useful to visualize the cost functions to understand why the optimization may have chosen a given solution and why computational times seem to differ between functions. Because it is difficult to visualize cost functions of three parameters, only the functions for the two sphere models are analyzed.

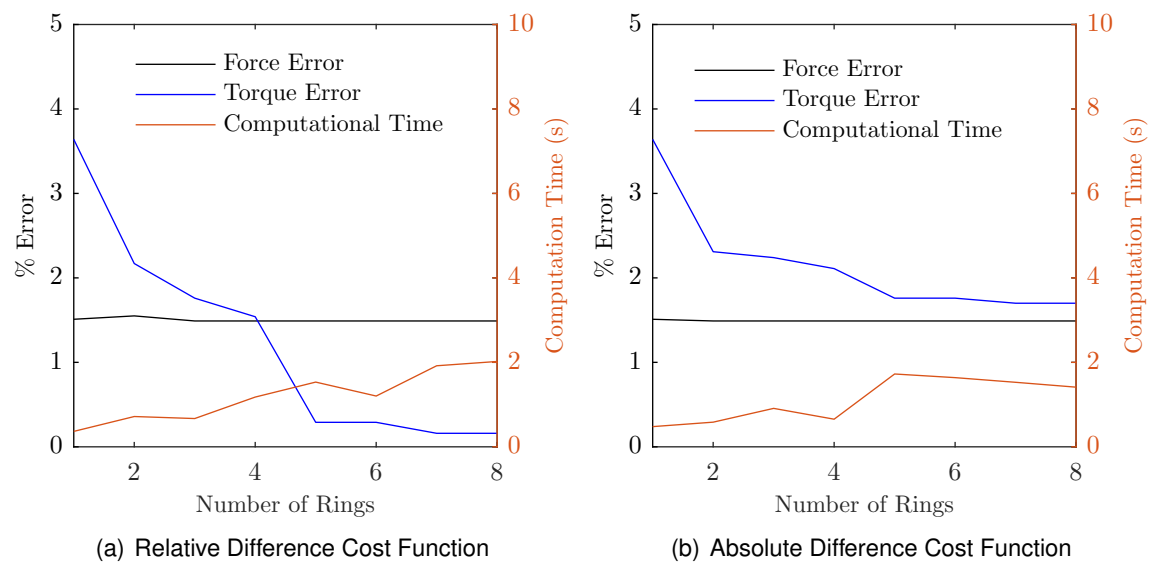


Figure 1.12: *Two Sphere VMSM Performance, With Capacitance Constraint*

The cost surface for the two sphere VMSM can be visualized as shown in Figure 1.13, where the darker hues indicates a lower — and thus more desirable — cost. The black line on the plot indicates the successive steps that the optimization under the relative difference cost function follows. In Figure 1.13(b), a gray line is plotted to indicate the space of all points that satisfy the capacitance constraint.

An important aspect of the cost surface is the gradient around the minima where the solution converges. Although it is somewhat difficult to identify with the provided visualization, the gradient around that minima is smaller than at other points on the surface. This can make convergence on a solution difficult, which may explain why errors sometimes increase after including more rings.

Figure 1.13(b) illustrates one of the strengths of using the capacitance constraint: fast convergence on a solution. Because the search space has only one degree of freedom, it finds the local minima very quickly. Only one point, the initial condition, lies outside the minima where the optimized solution is found. It is not coincidental that the optimizer converged on a solution for this constrained case more quickly than any other case analyzed. Due to the capacitance constraint, the optimizer need only find the local minima on the capacitance line, rather than on an entire plane. A similar scenario likely exists when constraining the search space for the three sphere from a volume to a plane.

1.1.1.2.4.6 Summary of Cases

Table 1.2 lists the best fit each cost function achieved in addition to the fit from the baseline geometric parameters. Importantly, the new optimization methods provide MSM solutions in less than half the time previously required while avoiding hand tuning of initial conditions. This increased speed does not seem to have much cost associated with it, as errors are equivalent to or better than the baseline parameters. Even faster computational times, typically about half of the values listed here, can be achieved at an increase to the force and torque errors. This speed increase in determining suitable MSM parameters is particularly promising for future work that will consider larger numbers of MSM spheres or allow spheres to be generally distributed about the object geometry. Both scenarios will involve a larger number of MSM parameters which is more

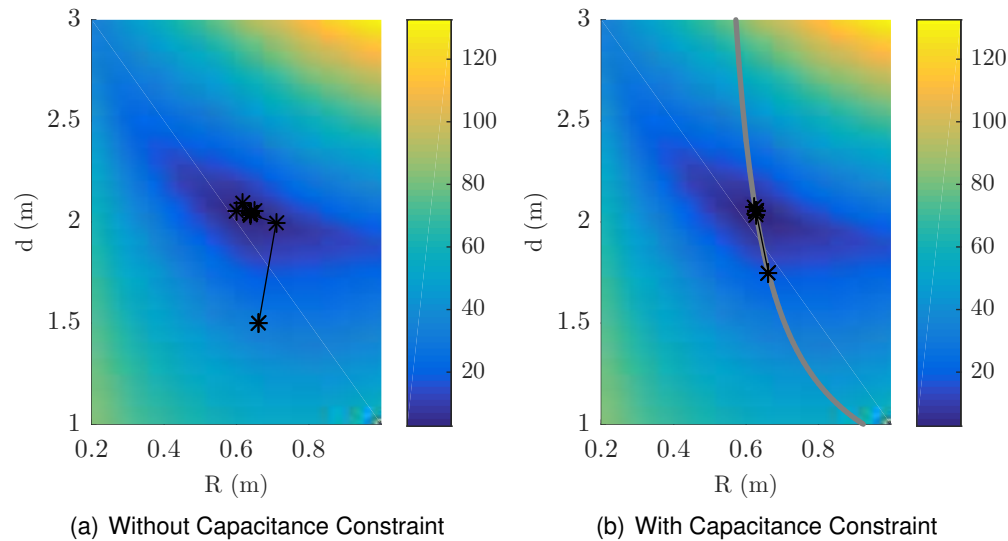


Figure 1.13: *Two Sphere Model Cost Surfaces*

Table 1.2: *Comparison of Optimized Parameters*

Cost Function	Force Error (%)	Torque Error (%)	Computational Time (sec)	Number of Rings Used
3 Sphere 3 Param. Abs. Difference	1.10	1.22	5.38	7
3 Sphere 3 Param. Rel. Difference	1.08	0.14	4.80	7
3 Sphere 2 Param. Abs. Difference	1.45	1.22	4.21	7
3 Sphere 2 Param. Rel. Difference	1.46	0.15	4.21	7
2 Sphere 2 Param. Abs. Difference	1.19	1.73	2.72	8
2 Sphere 2 Param. Rel. Difference	1.13	0.14	2.89	7
2 Sphere 1 Param. Abs. Difference	1.49	1.70	1.41	8
2 Sphere 1 Param. Rel. Difference	1.49	0.16	1.92	7
Baseline Geometric Parameters	1.47	1.18	9.1 ⁶	N/A

taxing on the setup optimization process.

These results show that automated geometry optimization is indeed possible using the VMSM. It should be noted that cost functions that generate very small errors should not be assumed to be the best function. Recall that the truth model is based on a commercial electrostatic FEA tool, which is subject to numerical error. Additionally, the percentage errors of even the worst fits do not go beyond 4%; in actual scenarios involving electrostatic charging, uncertainties in the environment may very well be larger than any inaccuracies introduced by these optimizations. Consequently, the determination of the “best” cost function should weigh other factors, with computational time being the most likely.

There is a noticeable decrease in torque error when using the relative difference cost function when compared to the absolute difference cost function. While the exact reasons for this trend are as yet unclear, it is an important consideration because it can provide more accurate results with minimal increase in computation time.

In comparing computational time, there is a marked advantage when using the capacitance constraint, as it reduces the search space by an entire DOF. In addition the speeding up compu-

tation, the capacitance constraint implies accurate force prediction at larger distances due to the inverse square law reducing distant objects to single point charges. While the torque solution may be slightly less accurate due to the lost DOF, the overall errors are still not very large, particularly when considering the uncertainties inherent in space missions.

1.1.1.2.5 *Far-Field Probe Radii Conditioning*

The simple case of a sphere and cylinder is a good starting point for automated VMSM optimization. As the project begins to include more complex shapes the probe must move farther away. This allows far-field behavior to be enforced through capacitance and other constraints. Placing the probe very far from the target object (>20 meters) yields counter-intuitive results, i.e. the Maxwell force deviated by many tens or hundreds of percent from the point force formula, which ought to hold in the far field. It is thought that this is an error on Maxwell's part and is due to grid refinement issues.

In an attempt assuage these concerns, the probe radius was varied in the far field, where we would expect minimal departure from the point force formula, and the results were analyzed. Better matching to the point force formula was found if the probe sphere increased in size as it moved farther away. For each new shape, such as the box and panel model, the probe radius that yielded a force closest to the point force formula was recorded at various far-field distances, and fit with a parabola. This parabola was used to compute the probe radius for all the large number of maxwell runs at varying distances.

1.1.1.2.6 *E-Field Matching*

Using Maxwell as a truth model for force and torque matching has many difficulties: it takes long to compute, and gives un-intuitive and possibly un-physical results in many circumstances. Additionally, there are questions about the effect of the probe radius on the accuracy of the result. One method for bypassing the last issue is to remove the probe entirely, and measure the electric fields in the vicinity of the target rather than the force and torque on it.

This removes any question of the influence of the probe on the accuracy of the result, but introduces another question: Are MSM models produced without a nearby charged objects sufficient to predict force and torque in situations where there is a nearby charged object? There are two effects that will move charge within a conductor, the conductor's own voltage and geometry, and a strong electric field caused by a nearby charged object. In strong electric fields, the charge will be pushed to one or the other side of a conducting body, and the voltage and offset of center of mass from center of charge in the target will cause the charge to accumulate on different areas of the spacecraft. Measuring electric fields in the absence of another charged object only tests this later effect.

Further research will investigate whether VMSM models found by optimizing against the electric fields will also perform well in predicting force and torque in the charged 2 body problem. Obtaining E-fields from Maxwell has been tried, with the software developer support, but the results were only very rough measures. Current work is investigating obtaining smooth E-fields using SMSM models to generate the truth data to which the VMSM models are fitted.

1.1.1.3 **Validate MSM on Multiple Shapes**

While fitting research continues of the cylinder problem as a convenient upper-stage like prototype configuration, work has also progressed in applying the MSM fitting techniques to non-cylindrical

shapes. This sections provides updates regarding this on-going work and illustrates the promising results founds regarding using low-number of spheres to model complex E-field behaviors.

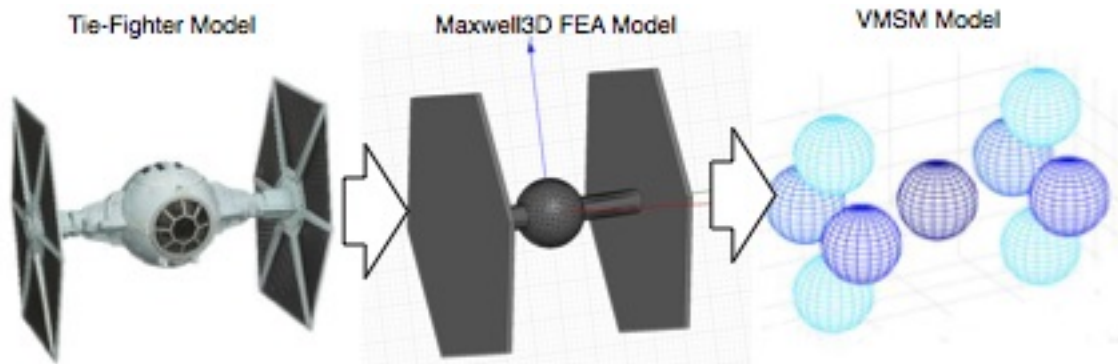


Figure 1.14: Illustration of how a Tie-Fighter Model is converted first to an FEA, then an MSM Model.

1.1.1.3.1 Fitting VMSM to a Star Wars Tie-Fighter

As an illustrative example of how this MSM-fitting technique can be applied to general shapes, the undergraduate researcher Christine Reilly chose to see how well she could fit the E-field about a Star Wars Tie-Fighter model, shown in Figure 1.14, to a VMSM model. This was a great outreach project, for which Christine earned a best-presentation award as a Discovery Learning Apprentice. A simplified finite element was created in Maxwell3D to create a cluster of E-force evaluations with respect to a spherical probe. She used the general MSM fitting code she was co-developing in Matlab to then the E-forces to a 9-sphere MSM model. Note that this shape appears general at first glance, but there there several symmetries that can be exploited. For example, the left and right panels are mirrored, thus the sphere placements on each is identical. Within a panel the 4 spheres are constrained to be on a circle with equal distance between them. Further, the last 9th sphere is constrained to be at the center of the craft, but have an unknown radius.

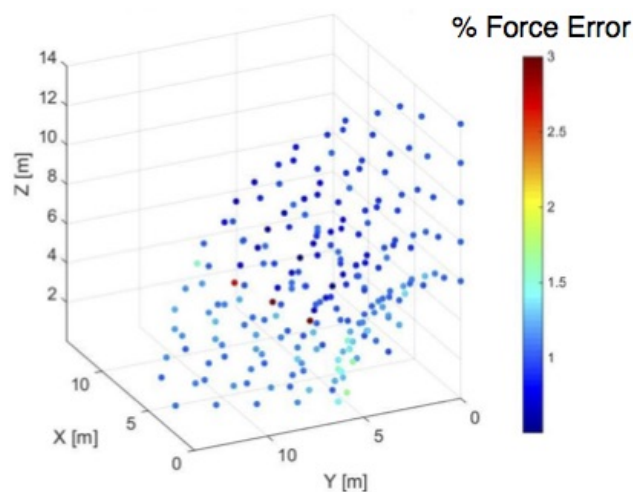


Figure 1.15: 9-Sphere VSMSM fitting error

The force fitting method outlined earlier is applied here, and achieved good results shown in

Figure 1.15. The mean force fitting errors were about the 1-1.5% level. This remarkable fitting is due to the larger number of spheres employed in this VMSM model, as well as all force measurements being taken outside of the two deflector panels.

This example MSM models illustrates how sub-component symmetries can be exploited to reduce the MSM optimization search space, and yield very practical answers. Consider that each sphere has a general 3D location, and a radius, that is 4 degrees of freedom (DOFs). Thus, if an unconstrained optimization is setup, with 9 spheres the optimizer is searching for $9 \times 4 = 36$ DOFs. With the above mentioned constraints applied, the center sphere has an unknown radius, but known location. The 8 spheres in the left and right panels all have the same radius, thus a single radius DOF. Their locations are dictated through a common radius relative to the prime axis, but know location on this circular. Thus, instead of 36 DOFs to search for, this setup was obtained searching for only 3 DOFs. Searching for such constraints in general shapes drastically speeds up the optimization, and helps also with robustness.

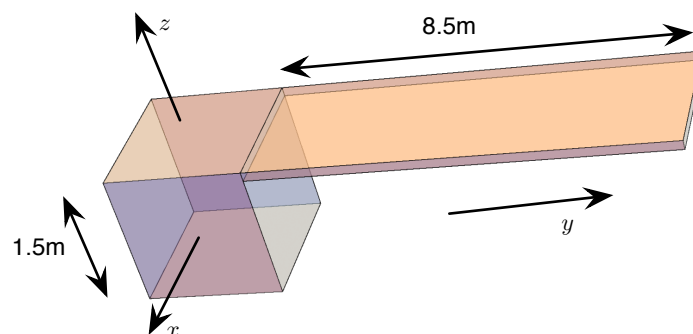


Figure 1.16: *Illustration of a Box-Panel Approximation of a GOES-Like Spacecraft Model*

1.1.1.3.2 Fitting VMSM to a Box-Panel Spacecraft

Next, a more detailed study is presented on how well the VMSM method can be applied to a very asymmetric spacecraft shape. The GOES spacecraft has a compact, box-like hub, and a single large solar array protruding to one side. This creates a strong asymmetry which is investigated in this study. The prototype box-panel model employed is shown in Figure 1.16. This discussion is broken up into 2 components. First, the results and challenges of fitting the VMSM model to the Maxwell3D E-force data is presented, following by a preview of on-going research with a new method of developing the VMSM model that is based on using a higher fidelity Surface MSM or SMSM model.

1.1.1.3.2.1 VMSM Model from Maxwell3D FEA data

ANSYS Maxwell3D is a commercial FEA solver that has been used to generate the array of E-force evaluations. The box-panel model shown in Figure 1.16 was created inside Maxwell3D. A spherical probe shape was used to generate an E-force at a range of locations. With this very elongated box-panel model, a challenge quickly manifested itself with regard to the spherical probe size. As we are fitting the spacecraft MSM in relation to a single sphere, the probe size cannot be too large or induced effects will corrupt the fitting process. However, if the sphere is too small, the the FEA grid-refinement process will have challenges. The results shown below are obtained where the probe radius is held smaller (around 0.25m) near the spacecraft shape, and increased

to over a meter for the far-off distances. The process of tuning the radii is challenging and time-consuming, something we are trying to avoid. The second sub-section talking about the SMSM based fitting approach yields a very promising, simpler setup and optimization process. All the fitting results obtained in this section are produced using the commercial Mathematica and its built-in `NMinimize[]` function. Further, as discussed earlier in this report, it is beneficial to fit the MSM model to the probe locations close to the spacecraft. The E-field variations due to the non-spherical shapes are more pronounced here, making it easier for the optimizer to determine a solution. Further, as the E-forces drop off sharply with larger separation distances, the equality of the Maxwell3D compute E-force degrades quickly. The FEA convergence tolerance cannot be set small enough to produce more than ball-park values of these very small forces at a distance. This will manifest itself when the VMSM fit quality is discussed later on. In the results below, only the data points up to 15 meters from the spacecraft box center are included in the fitting optimization, while all data points are used in the fit evaluation process.

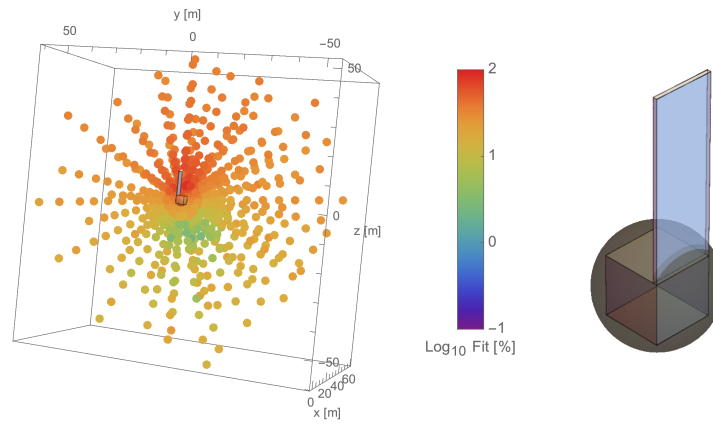
Figure 1.17 illustrates the fitting results if the box-panel data is fit to a single sphere. As a baseline results, Figure 1.17(a) fits the data to a single sphere constrained to the center of the box shape. The only DOF here is the sphere radius. E-force data points are taken out to about 50 meters, or about 6-7 times the craft size. The mean E-force and torque fit is shown using a logarithmic scale. The color bar shows the percent error colors using a base 10 scale. Thus, dark green is near 0 here, which represents $10^0 = 1\%$ fitting error. The yellow regions are around 10%, orange are 10's of percent and reds are 100% and above. Using a box-centered single-sphere only provide a marginal MSM model. Notice the green region below the spacecraft model which indicates errors less than 10%. This is due to this MSM model being fit to data out to 15 meters only. Further away from the craft the errors increase as this fit is not constrained to match the self-capacitance. The error along the slender solar panel are poorly approximated. This baseline example illustrates the challenging of fitting a sphere.

The next scenario assumed a single sphere where the radius R , and location coordinates y and z are unknown, shown in Figure 1.17(b). The fit quality now improves greatly, with many errors ranging less than 10% below the craft, and in the 10's of percent in the solar panel region. In Figure 1.17(c) the same optimization process is repeated, but the self capacitance value of the VMSM model is constrained to match the value obtained from Maxwell3D. Matching the self-capacitance improves some of the far-out data points. however, with the Maxwell3D issues of evaluating these far off forces, this impact is hard to see in these fit plots.

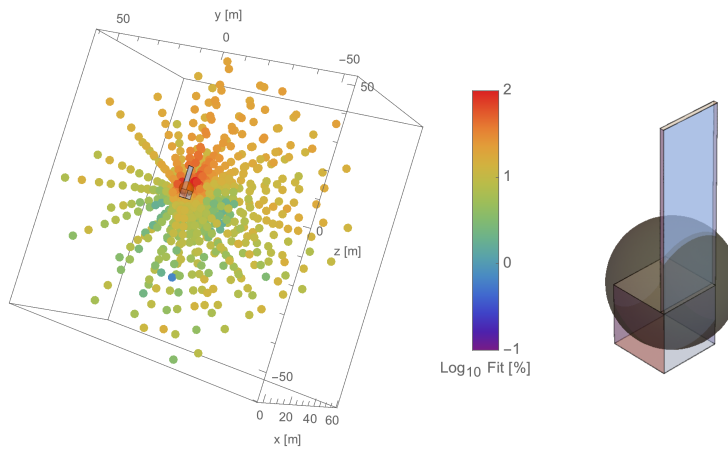
Figure 1.18 shows the results if 2 spheres are used to fit the E-forces and torques. The overall errors improve significantly to less than 10% except for the very near data points, as expected. Here induced effects are not well resolved with a low-order 2-sphere model.

The fit quality of a range of VMSM solutions are compared in Figure 1.19. Here the average fit quality is determined for all data points at the same radius r from the spacecraft center, as illustrated in Figure 1.20. The blue line labeled "1-sphere" shows the case where a single sphere is fitted to the spacecraft hub center, and the radius is optimized to fit the data. The errors range here around 25-35%, and decrease initially as the distance increases and the E-field is acting more like that of a sphere. However, as this optimization doesn't match the self-capacitance, the far off measurements are consistently off the Maxwell data.

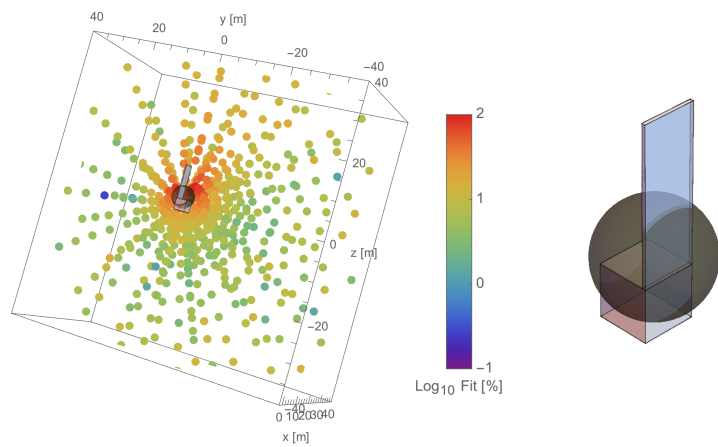
The orange line, labeled "1-sphere shifted" shows the result shown in Figure 1.17(b). The close data points have a much better fit, but the far off data points don't converge to the Maxwell data either. The green line, labeled "1-sphere (c)", shows the result of optimizing a single sphere centered at the hub, but the radius is determined to match the self-capacitance value. This is equivalent to the effective sphere representation discussed in Reference 7. The nearby data fit isn't as good as the other single sphere methods, but by matching the self-capacitance, the large



(a) Single Sphere Centered on Box

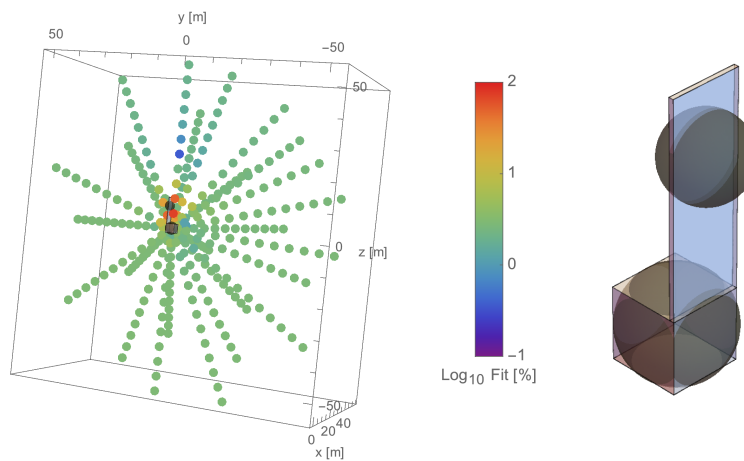


(b) Single Sphere Optimized

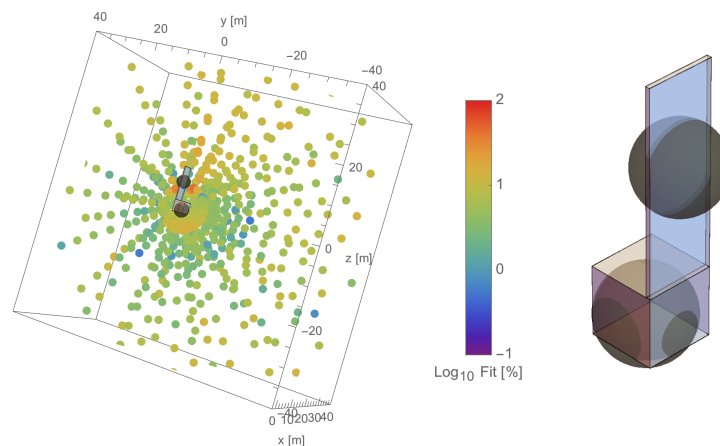


(c) Single Sphere Optimized Constraint to Self-Capacitance

Figure 1.17: Single Sphere VMSM Models Matched to the Maxwell3D Data for the Box-Panel Spacecraft Shape.



(a) Two-Sphere Optimized



(b) Two-Sphere Optimized Constraint to Self-Capacitance

Figure 1.18: *Two-Sphere VMSM Models Matched to the Maxwell3D Data for the Box-Panel Spacecraft Shape.*

distance data is approaching the Maxwell data. The best 1-sphere fit is obtained with the red line labeled “1-sphere shifted (c)” shown in Figure 1.17(c). The near data is only slightly worse than the “1-sphere shifted” case, but the far off data is much better as the self-capacitance is matched.

The 2-sphere cases are shown in the blue and brown line. Again the unconstrained solution provides a slightly better fit for the data range over which the fit is performed (up to a probe distance of 15 meters). For larger distance the errors converge to the common offset. Note a general issues here trying to evaluate the fit quality with the Maxwell data. For probe locations close to the spacecraft, the numerical E-forces are large enough to be easily resolved, and thus have a higher accuracy level. However, are larger distances the E-forces become very small, leading to strong challenges for the FEA solution to resolve these small values across finite element dimensions. This is why in all these fits the errors begin to increase with larger probe distance instead of converging to zero if the self-capacitance is matched. This is an issue with the Maxwell3D “truth data” not being very good at these location. Maxwell3D only provides rough approximations of these small forces. The following section discusses a very promising method to overcome some of these challenges of using a FEA solution by itself as the truth model.

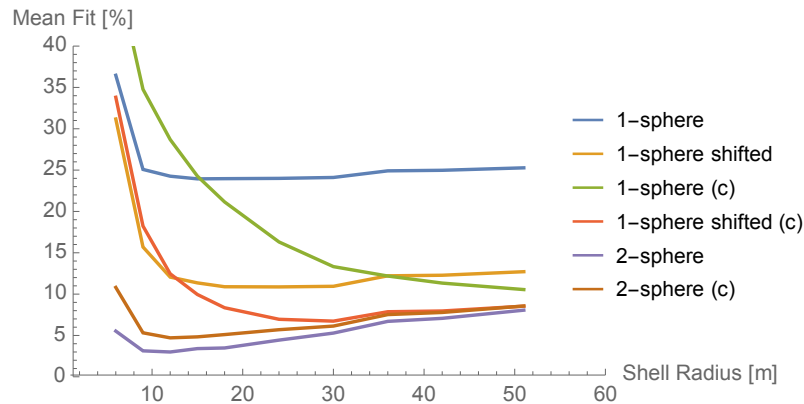


Figure 1.19: Comparison between Maxwell Fitted VMSM Models

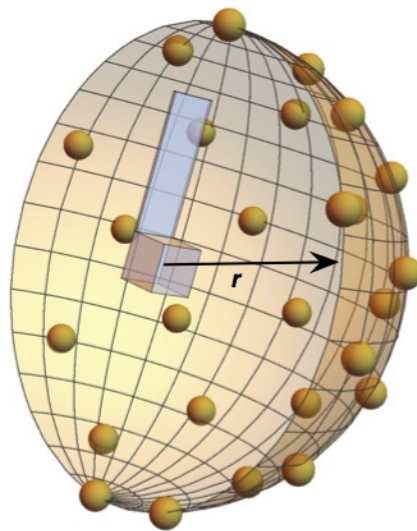


Figure 1.20: Illustration of Average Shell Fitting Value

1.1.1.3.2.2 VMSM Model from High-Fidelity SMSM data

Fitting MSM models to match computationally FEA evaluated solutions from Maxwell3D has proven successful in developing elegant low-order VMSM solutions. However, this process has also displayed several challenges. The following sections illustrate some work-in-progress on developing a revised VMSM fitting process that is simpler to setup, faster to converge, and provides better fit quality measures at larger distances. The challenges of fitting E-forces to FEA solutions include:

1. The FEA solution is not smooth, contains a range of numerical artifacts.
2. No method to export the E-fields well from the FEA solutions. All software developer suggested solutions yielded very rough E-field estimates.
3. To evaluate E-forces, two bodies must be simulated in the FEA such as the spacecraft shape and a spherical probe. The probe size, if not selected well, impacts the data quality.
4. FEA E-force solutions at larger distances are very challenging to get accurate. The relative accuracy decreases as the E-forces at a distance drop off rapidly with $1/r^2$.

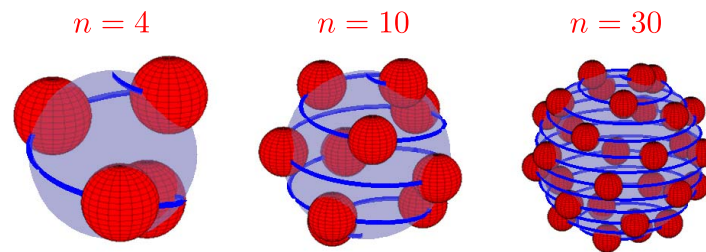


Figure 1.21: Illustration of Equal Separation Distance Surface Spheres being Placed on a Single Sphere

A revised VMSM methods are being investigated, and the following results are some early indicator of the promise of these new approaches. The FEA is very good at

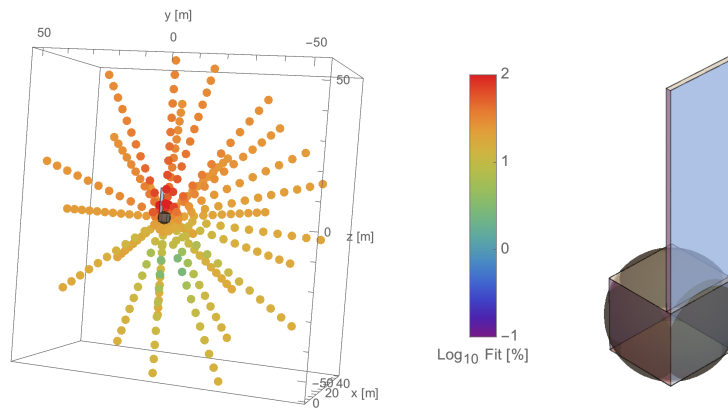
1. Computing the self-capacitance of the space object being modeled.
2. Evaluating the E-forces within 1-3 craft radii where the forces are larger.

A new approach being considered replaces the FEA truth data with data from a Surface MSM or SMSM model. The following section discusses progress in developing software to setup SMSM models on prototype shapes. The spacecraft shape surface is populated with a large number of equal-radius spheres which are placed roughly equally spaced apart as shown in Figure 1.21.⁶ The FEA self-capacitance C_s value is used to select a SMSM sphere radius such that the MSM self-capacitance matches C_s from the FEA solution. Having a very high-fidelity SMSM model with 100's of spheres provides a very accurate and smooth estimate of the actual E-forces about a general shape. The computational E-force evaluation with 100's of spheres is not fast, as a equivalent matrix inverse must be performed. However, as this high-fidelity SMSM model is not used for a dynamic simulation, but rather to generate a static E-force data set, the speed of the SMSM evaluation is less a concern. In particular, compared to running a sweep of FEA solutions to generate the data, the high-fidelity SMSM approach is still 10x faster.

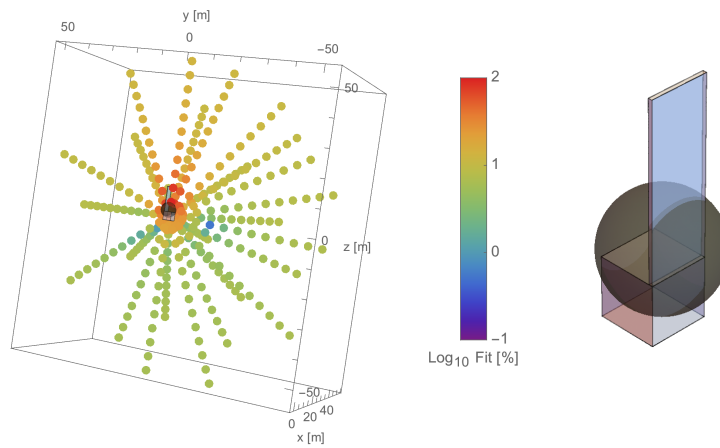
Next, the earlier outline VMSM fitting approach is applied to this SMSM derived truth data. This data doesn't have any artifacts due to finite spacial element sizes, or convergence issues with vanishingly small forces.

Some early illustrative results are shown in Figure 1.22 and 1.23. The same setups are repeated as for the Maxwell fitted data in the previous sub-section. Fitting a single sphere to the hub center, shown in Figure 1.22(a), provides a similar baseline result where significant E-force model errors are found in particular along the solar-panel direction. Allowing 1-sphere location to be optimized as well, shown in Figure 1.22(b), greatly improves the overall fit near the spacecraft. However, with the more accurate SMSM long-distance E-force predictions, it is now more evident that this solution doesn't converge well at large distances. In contrast, if the 1-sphere radius and location are optimized subject to matching the spacecraft FEA self-capacitance, the good fits near the spacecraft are retained while also seeing the fit quality improve with larger distances. This is the expected behavior with the MSM solutions, as at larger separations all finite objects with have E-fields that approach that of a sphere. However, the FEA numerical solution issues at these distances prevented this trend from being numerically validated.

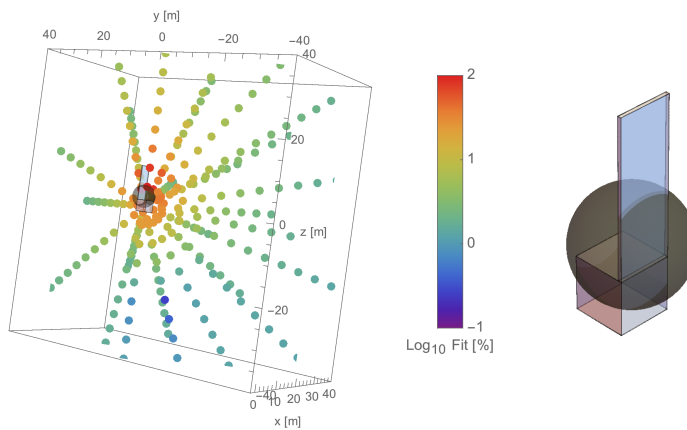
Early results fitting a 2-sphere solution to the SMSM data are shown in Figure 1.23. The solution in Figure 1.23(a) is the result of a constraint-free optimization, while Figure 1.23(b) shows the result of an optimization that constrains the VMSM self-capacitance to match the FEA self-capacitance. Note that the 2 solutions are essentially equivalent in their MSM sphere locations



(a) Single Sphere Centered on Box

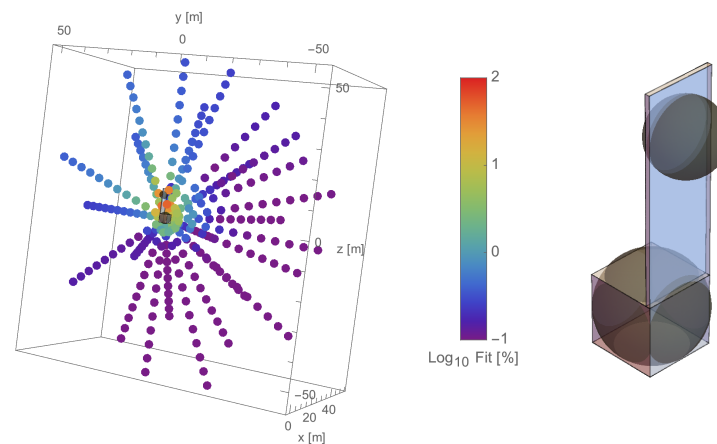


(b) Single Sphere Optimized

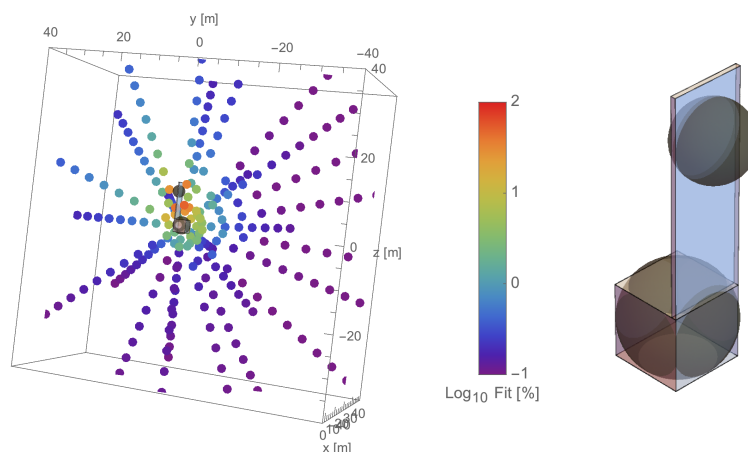


(c) Single Sphere Optimized Constraint to Self-Capacitance

Figure 1.22: Single Sphere VSM Models Matched to the SMSM Data for the Box-Panel Spacecraft Shape.



(a) Two-Sphere Optimized



(b) Two-Sphere Optimized Constraint to Self-Capacitance

Figure 1.23: *Two-Sphere VMSM Models Matched to the Maxwell3D Data for the Box-Panel Spacecraft Shape.*

and radii, and the quality of their E-force fitting. This is a very promising result as it indicates that fitting to the very “clean” SMSM data provides a MSM solution that automatically matches the expected self-capacitance. This encouraging result will need to be explored further by investigating higher number of MSM sphere fits, as well as considering a range of shapes. The un-constrained optimization runs faster and is easier to setup than the constrained optimization. Further, in this optimization the data is fit up to shells of 15 meters. The less data is required in the fitting, the faster the fit will be. In Mathematica, these 2-sphere fits took over 30 minutes to complete. Future work will investigate the impact of fitting to smaller sub-sets of data close to the spacecraft.

The average E-force fitting quality across a shell of data points is shown in Figure 1.24. Generally a similar trend is observed as with the FEA-fitted data, but the error predictions are now smoother (no FEA discretization corruptions) and more accurate at longer distances. The “1-sphere” fit centered on the hub has the errors converge to about 23% as the self-capacitance is not matched. The effective sphere model “1-sphere (c)” matches the self-capacitance, and produces better and better fits at larger distances as a result. Allowing the sphere location to be optimized again strongly improves the overall fit quality. As expected, the “1-sphere shifted” result

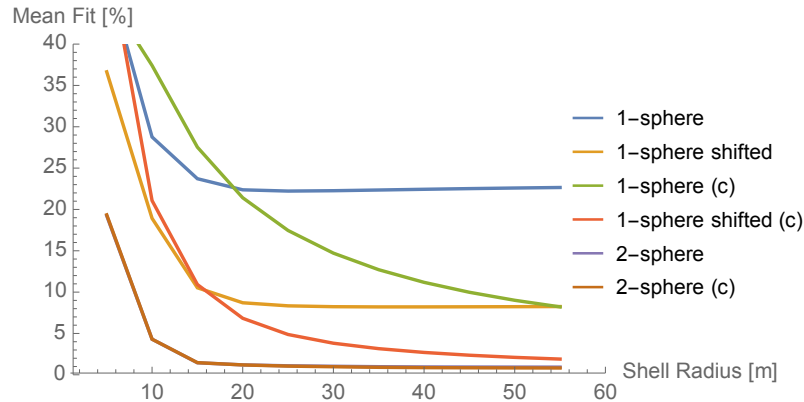


Figure 1.24: Comparison between SMSM Fitted VMSM Models

is slightly better than the “1-sphere shifted (c)” result as closed distances as the first is optimized only over data up to 15 meters. However, the self-capacitance constrained solution is superior at larger distances. Finally, the 2-sphere fit qualities as essentially identical as both optimizations yielded the same result. With 2-spheres the fit quality is good near the craft with 5-15% errors, and excellent at larger distances with errors far less than 1%.

1.1.2 Surface-MSM Setup Optimization

SMSM uniformly places many spheres of equal radius all over the surface of a spacecraft, and then varying the radii of all spheres until the self capacitance of the MSM model matches that of the actual object. Functions are written to equally place points on the surface of a rectangle, cylinder, and sphere. These pieces can be combined to create many complex prototype spacecraft shapes. The self capacitance of simple objects such as spheres, ellipsoids, and disks are known analytically, and there are good empirical approximations for the self capacitance of a rectangle. More complex shapes, such as a general spacecraft, must be modeled with an FEA program, such as Maxwell, to find the capacitance.

The problem of placing points uniformly on the surface of a sphere is well-studied in computer science.⁸ A spiral based on the golden spiral is inscribed on the surface of a sphere much like a candy cane. Points are placed on this line at longitudes separated by the golden angle $\phi = \pi(3 - \sqrt{5})$. This is shown below for 50 spheres. The color indicates the charge on that sphere if the object were uniformly charged. Notice that the color scale indicates very little change in the actual surface charge density, which is analytically constant for a sphere.

For a cylinder, a 2D version of the golden spiral detailed above is used for the ends and hexagonal packing is used for the body. This is shown using a total of 50 spheres in the figure below.

To make the rectangle four inputs are required: the length L_x , width L_y , approximate separation dx , and self capacitance C . The rectangle is divided into a grid with n_x and n_y points along its length and width. n_x and n_y are defined below:

$$n_x = \text{round}(L_x/dx), \quad n_y = \text{round}(L_y/dx) \quad (1.28)$$

Then the Matlab function `meshgrid()` is used to make matrices for this grid. These matrices are then vectorized and a equally sized vector of zeros is added to give the 3D positions of each sphere in the model. Lastly, the radius of each sphere is varied by the Matlab program `fsolve()` to match the self capacitance of the MSM model to that of the actual object.

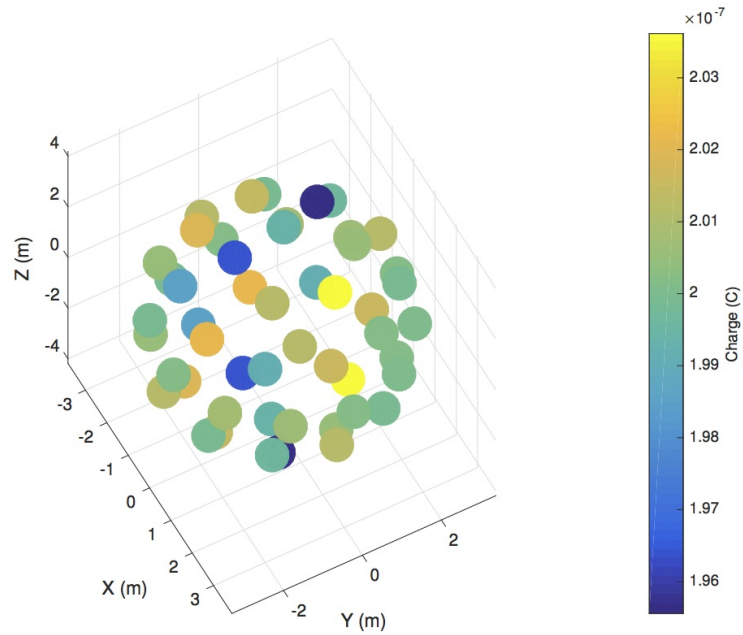


Figure 1.25: Golden spiral is used to make SMSM for sphere

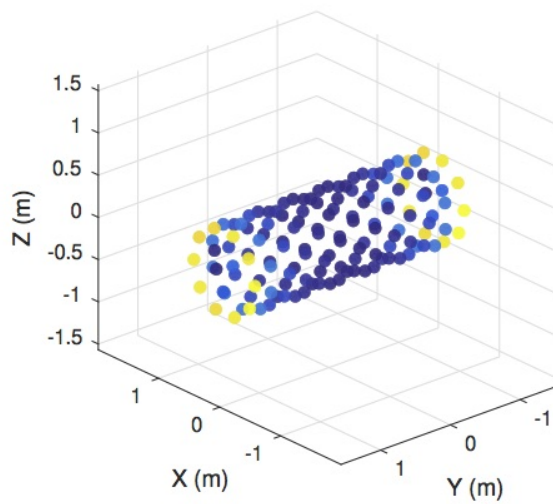


Figure 1.26: Golden spiral is used to make SMSM for cylinder

The completed MSM model with correctly sized spheres and color indicating the charge on each sphere for a square plate in Figure 1.27. As one can see, more charge (shown as color) accumulates near the corners of the plate.

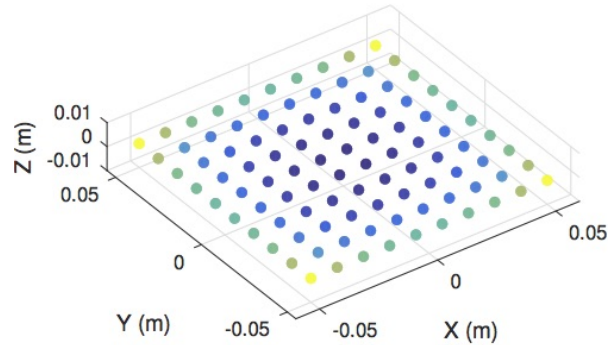


Figure 1.27: Conducting rectangle modeled using Automated SMSM

1.1.3 Comparison to Appropriate Fidelity Models (AFMs)

AFMs were created in an attempt to find metrics other than force and torque percentage error between a MSM model and Maxwell. However, they have grown into an exciting field of their own. They are a parallel method to MSM for force and torque prediction that is typically less accurate, but gives greater analytic insight. Additionally, they offer numeric constraints that can be used in MSM parameter optimization.

The AFM process is two-fold. The first step is to derive approximate expressions for the force and torque on a charged body. Truncating an infinite series to second order leaves three measures of the charge distribution: the scalar charge Q , the dipole q_{sep} and the charge tensor $[Q]$. The second step is to find out how to predict these measures from knowledge of the voltage or each craft and their separation. This is done using a table of susceptibilities that capture the approximate influence of voltage and ambient field on the three measures, from which the force and torque can be predicted.

1.1.3.1 Development of Appropriate Fidelity Models (AFMs)

The force and torque on a charged body can be found by integrating the differential force across it. The differential force on body 2 is given by

$$d\mathbf{F}_2 = \frac{dq_1 dq_2 \mathbf{R}}{4\pi\epsilon_0 R^3} \quad (1.29)$$

where \mathbf{R} points from dq_1 to dq_2 . The separation vector can be expressed from body vectors and a vector between the center of mass of each body $\mathbf{R} = \mathbf{R}_c + \mathbf{r}_2 - \mathbf{r}_1$ as shown in Figure 1.28. Using this substitution makes the differential force

$$d\mathbf{F}_2 = \frac{dq_1 dq_2 \mathbf{R}_c + \mathbf{r}_2 - \mathbf{r}_1}{4\pi\epsilon_0 \|\mathbf{R}_c + \mathbf{r}_2 - \mathbf{r}_1\|^3} \quad (1.30)$$

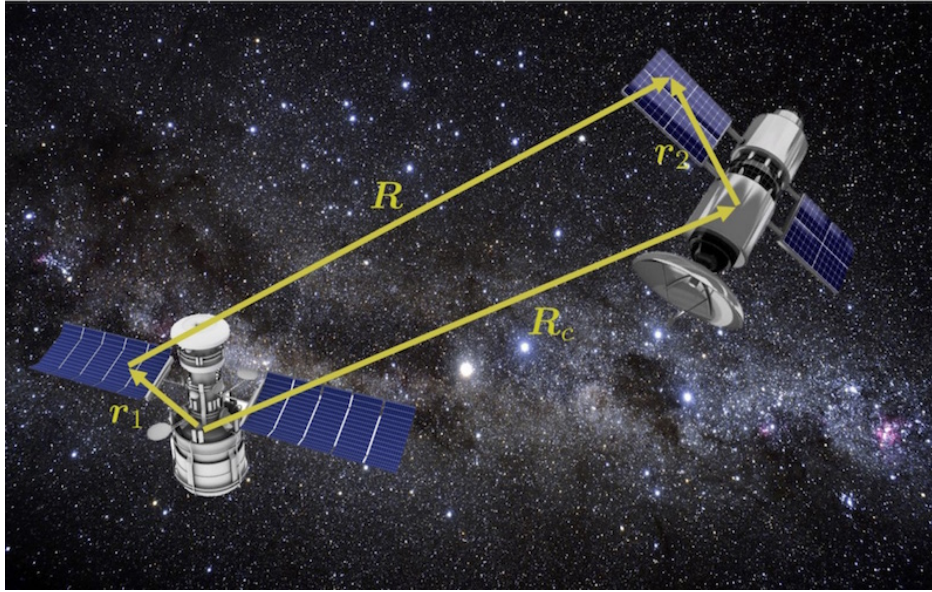


Figure 1.28: Coordinate frames for two body electrostatic force and torque derivation

The denominator of this expression appears formidable, but it can be simplified using a binomial series. To do so the denominator must be in the form $(1 + x)^\alpha$, where x is a scalar. To do this, the denominator is dotted with itself and the square root is taken.

$$R^{-3} = (R_c^2 + r_1^2 + r_2^2 + 2(\mathbf{R}_c \cdot \mathbf{r}_2 - \mathbf{R}_c \cdot \mathbf{r}_1 - \mathbf{r}_2 \cdot \mathbf{r}_1))^{-3/2} \quad (1.31)$$

if R_c is assumed to be larger than r_1 or r_2 , it can be divided out to leave a 1 and a collection of small terms:

$$R^{-3} = \frac{1}{R_c^3} \left(1 + \frac{r_2^2}{R_c^2} + \frac{r_1^2}{R_c^2} + \frac{2}{R_c^2} (\mathbf{R}_c \cdot \mathbf{r}_2 - \mathbf{R}_c \cdot \mathbf{r}_1 - \mathbf{r}_2 \cdot \mathbf{r}_1) \right)^{-3/2} \quad (1.32)$$

All of the small terms can be lumped into the small variable x and a second order binomial series can be used to approximate it;

$$\frac{1}{(1 + x)^{3/2}} = 1 - \frac{3}{2}x + \frac{15}{8}x^2 + \dots \quad (1.33)$$

Using this with the substitution $x = \frac{r_2^2}{R_c^2} + \frac{r_1^2}{R_c^2} + \frac{2}{R_c^2} (\mathbf{R}_c \cdot \mathbf{r}_2 - \mathbf{R}_c \cdot \mathbf{r}_1 - \mathbf{r}_2 \cdot \mathbf{r}_1)$ and removing any terms higher than second order gives the differential force as

$$d\mathbf{F}_2 = \frac{dq_1 dq_2}{4\pi\epsilon_0 R_c^3} (\mathbf{R}_c + \mathbf{r}_2 - \mathbf{r}_1) \left(1 - \frac{3r_1^2}{2R_c^2} - \frac{3r_2^2}{2R_c^2} - \frac{3(\mathbf{R}_c \cdot \mathbf{r}_2 - \mathbf{R}_c \cdot \mathbf{r}_1 - \mathbf{r}_2 \cdot \mathbf{r}_1)}{R_c^2} + \frac{15((\mathbf{R}_c \cdot \mathbf{r}_2)^2 + (\mathbf{R}_c \cdot \mathbf{r}_1)^2 - (\mathbf{R}_c \cdot \mathbf{r}_1)(\mathbf{R}_c \cdot \mathbf{r}_2))}{2R_c^4} \right) \quad (1.34)$$

1.1.3.1.1 Force Derivation

The total force on body 2 is found by integrating the differential force in Eq. (1.34) as shown below:

$$\mathbf{F}_2 = \frac{1}{4\pi\epsilon_0 R_c^3} \int_{B_1} \int_{B_2} (\mathbf{R}_c + \mathbf{r}_2 - \mathbf{r}_1) \left(1 - \frac{3r_1^2}{2R_c^2} - \frac{3r_2^2}{2R_c^2} - \frac{3(\mathbf{R}_c \cdot \mathbf{r}_2 - \mathbf{R}_c \cdot \mathbf{r}_1 - \mathbf{r}_2 \cdot \mathbf{r}_1)}{R_c^2} + \frac{15((\mathbf{R}_c \cdot \mathbf{r}_2)^2 + (\mathbf{R}_c \cdot \mathbf{r}_1)^2 - (\mathbf{R}_c \cdot \mathbf{r}_1)(\mathbf{R}_c \cdot \mathbf{r}_2))}{2R_c^4} \right) dq_2 dq_1 \quad (1.35)$$

This equation will be broken into three parts: the terms resulting from the \mathbf{R}_c , \mathbf{r}_1 , and \mathbf{r}_2 in the first set of parentheses. The first one is denoted \mathbf{F}_{2_0} and is given below:

$$\begin{aligned} \mathbf{F}_{2_0} &= \frac{\mathbf{R}_c}{4\pi\epsilon_0 R_c^3} \int_{B_1} \int_{B_2} \left(1 - \frac{3r_1^2}{2R_c^2} - \frac{3r_2^2}{2R_c^2} - \frac{3(\mathbf{R}_c \cdot \mathbf{r}_2 - \mathbf{R}_c \cdot \mathbf{r}_1 - \mathbf{r}_2 \cdot \mathbf{r}_1)}{R_c^2} + \frac{15((\mathbf{R}_c \cdot \mathbf{r}_2)^2 + (\mathbf{R}_c \cdot \mathbf{r}_1)^2 - (\mathbf{R}_c \cdot \mathbf{r}_1)(\mathbf{R}_c \cdot \mathbf{r}_2))}{2R_c^4} \right) dq_2 dq_1 \quad (1.36) \\ &= \frac{\mathbf{R}_c}{4\pi\epsilon_0 R_c^3} \left[Q_1 Q_2 - \left(\frac{3}{2R_c^2} \int_{B_1} r_1^2 dq_1 \int_{B_2} dq_2 \right) - \left(\frac{3}{2R_c^2} \int_{B_2} r_2^2 dq_2 \int_{B_1} dq_1 \right) \right. \\ &\quad - \left(\frac{3}{R_c^2} \mathbf{R}_c \cdot \int_{B_1} dq_1 \int_{B_2} \mathbf{r}_2 dq_2 \right) + \left(\frac{3}{R_c^2} \mathbf{R}_c \cdot \int_{B_2} dq_2 \int_{B_1} \mathbf{r}_1 dq_1 \right) \\ &\quad + \left(\frac{3}{R_c^2} \int_{B_1} \mathbf{r}_1 dq_2 \int_{B_2} \mathbf{r}_2 dq_2 \right) + \left(\frac{15}{2R_c^4} \int_{B_1} dq_1 \int_{B_2} (\mathbf{R}_c \cdot \mathbf{r}_2)^2 dq_2 \right) \\ &\quad \left. + \left(\frac{15}{2R_c^4} \int_{B_2} dq_2 \int_{B_1} (\mathbf{R}_c \cdot \mathbf{r}_1)^2 dq_1 \right) - \left(\frac{15}{2R_c^4} \int_{B_2} (\mathbf{R}_c \cdot \mathbf{r}_2) dq_2 \int_{B_1} (\mathbf{R}_c \cdot \mathbf{r}_1) dq_1 \right) \right] \quad (1.37) \end{aligned}$$

The definitions for Q , q_{sep} , and $[Q]$ presented in Reference 9 and the fact that $\int r^2 dq = \text{tr}([Q])/2$ are used to simplify the above equation.

$$\begin{aligned} &= \frac{\mathbf{R}_c}{4\pi\epsilon_0 R_c^3} \left[Q_1 Q_2 - \frac{3Q_2}{4R_c^2} \text{tr}([Q_1]) - \frac{3Q_1}{4R_c^2} \text{tr}([Q_2]) - \frac{3Q_1}{R_c^2} \mathbf{R}_c \cdot \mathbf{q}_2 + \frac{3Q_2}{R_c^2} \mathbf{R}_c \cdot \mathbf{q}_1 \right. \\ &\quad \left. + \frac{3Q_2}{R_c^2} \mathbf{q}_2 \cdot \mathbf{q}_1 + \frac{15Q_1}{2R_c^4} \int_{B_2} (\mathbf{R}_c \cdot \mathbf{r}_2)^2 dq_2 + \frac{15Q_2}{2R_c^4} \int_{B_1} (\mathbf{R}_c \cdot \mathbf{r}_1)^2 dq_1 - \frac{15}{2R_c^4} (\mathbf{R}_c \cdot \mathbf{q}_2)(\mathbf{R}_c \cdot \mathbf{q}_1) \right] \quad (1.38) \end{aligned}$$

To solve the last two integrals, the vector identity $(\mathbf{a} \cdot \mathbf{b})\mathbf{b} = ([\tilde{\mathbf{b}}][\tilde{\mathbf{b}}] + b^2[I])\mathbf{a}$ is applied to the term $(\mathbf{R}_c \cdot \mathbf{r})^2$ to yield $\mathbf{R}_c \cdot (\mathbf{R}_c \cdot \mathbf{r})\mathbf{r} = \mathbf{R}_c \cdot ([\tilde{\mathbf{r}}][\tilde{\mathbf{r}}] + r^2[I])\mathbf{R}_c = R_c^2([\tilde{\mathbf{r}}][\tilde{\mathbf{r}}] + r^2[I]) = R_c^2(-[Q] + \frac{1}{2}\text{tr}([Q]))$. The first part of the force is then given by

$$\begin{aligned} &= \frac{1}{4\pi\epsilon_0 R_c^3} \left[Q_1 Q_2 - \frac{3Q_1}{R_c^2} \mathbf{R}_c \cdot \mathbf{q}_2 + \frac{3Q_2}{R_c^2} \mathbf{R}_c \cdot \mathbf{q}_1 + \frac{3Q_2}{2R_c^2} \text{tr}([Q_1]) + \frac{3Q_1}{2R_c^2} \text{tr}([Q_2]) \right. \\ &\quad \left. + \frac{3}{R_c^2} \mathbf{q}_2 \cdot \mathbf{q}_1 - \frac{15Q_1[Q_2]}{2R_c^2} - \frac{15Q_2[Q_1]}{2R_c^2} - \frac{15}{2R_c^4} (\mathbf{R}_c \cdot \mathbf{q}_2)(\mathbf{R}_c \cdot \mathbf{q}_1) \right] \mathbf{R}_c \quad (1.39) \end{aligned}$$

The second part of the force is simpler because the \mathbf{r}_2 causes many terms to become 3rd order and are neglected.

$$\mathbf{F}_{2_2} = \frac{1}{4\pi\epsilon_0 R_c^3} \int_{B_1} \int_{B_2} \mathbf{r}_2 \left(1 - \frac{3(\mathbf{R}_c \cdot \mathbf{r}_2 - \mathbf{R}_c \cdot \mathbf{r}_1)}{R_c^2} \right) dq_2 dq_1 \quad (1.40)$$

Table 1.3: Force ordering matrix

	Q_1	q_1	$[Q_1]$
Q_2	$Q_1 Q_2 \mathbf{R}_c$	$\frac{3Q_2}{R_c^2} (\mathbf{R}_c \cdot \mathbf{q}_1) \mathbf{R}_c - Q_2 \mathbf{q}_1$	$\frac{3Q_2}{2R_c^2} \text{tr}([Q_1]) - \frac{15Q_2[Q_1]}{2R_c^2} \mathbf{R}_c - \frac{3Q_2}{R_c^2} ([Q_1] - \text{tr}([Q_1])) \mathbf{R}_c$
q_2	$(-\frac{3Q_1}{R_c^2} \mathbf{R}_c \cdot \mathbf{q}_2) \mathbf{R}_c + Q_1 \mathbf{q}_2$	$(\frac{3}{R_c^2} \mathbf{q}_2 \cdot \mathbf{q}_1 - \frac{15}{2R_c^4} (\mathbf{R}_c \cdot \mathbf{q}_2) (\mathbf{R}_c \cdot \mathbf{q}_1)) \mathbf{R}_c + \frac{3(\mathbf{R}_c \cdot \mathbf{q}_1)}{R_c^2} \mathbf{q}_2 - \frac{3(\mathbf{R}_c \cdot \mathbf{q}_2)}{R_c^2} \mathbf{q}_1$	
$[Q_2]$	$(\frac{3Q_1}{2R_c^2} \text{tr}([Q_2]) - \frac{15Q_1[Q_2]}{2R_c^2}) \mathbf{R}_c + \frac{3Q_1}{R_c^2} ([Q_2] + \text{tr}([Q_2])) \mathbf{R}_c$		

This can be evaluated as follows:

$$\mathbf{F}_{2_2} = \frac{1}{4\pi\epsilon_0 R_c^3} \left[Q_1 \mathbf{q}_2 - \frac{3}{R_c^2} \int_{B_1} \int_{B_2} \mathbf{r}_2 (\mathbf{R}_c \cdot \mathbf{r}_2 - \mathbf{R}_c \cdot \mathbf{r}_1) dq_2 dq_1 \right] \quad (1.41)$$

$$= \frac{1}{4\pi\epsilon_0 R_c^3} \left[Q_1 \mathbf{q}_2 - \frac{3Q_1}{R_c^2} \int_{B_2} \mathbf{r}_2 (\mathbf{R}_c \cdot \mathbf{r}_2) dq_2 + \frac{3}{R_c^2} \int_{B_2} \int_{B_1} (\mathbf{R}_c \cdot \mathbf{r}_1) \mathbf{r}_2 dq_2 dq_1 \right] \quad (1.42)$$

$$= \frac{1}{4\pi\epsilon_0 R_c^3} \left[Q_1 \mathbf{q}_2 - \frac{3Q_1}{R_c^2} \int_{B_2} ([\tilde{\mathbf{r}}_2][\tilde{\mathbf{r}}_2] - r_2^2 [I]) \mathbf{R}_c dq_2 + \frac{3}{R_c^2} \int_{B_2} \mathbf{r}_2 dq_2 \int_{B_1} (\mathbf{R}_c \cdot \mathbf{r}_1) dq_1 \right] \quad (1.43)$$

$$= \frac{1}{4\pi\epsilon_0 R_c^3} \left[Q_1 \mathbf{q}_2 + \frac{3Q_1}{R_c^2} ([Q_2] + \text{tr}([Q_2])) \mathbf{R}_c + \frac{3(\mathbf{R}_c \cdot \mathbf{q}_1)}{R_c^2} \mathbf{q}_2 \right] \quad (1.44)$$

The last of the three parts can be easily computed by switching the indices and adding a minus sign to \mathbf{F}_{2_2} .

$$\mathbf{F}_{2_1} = \frac{1}{4\pi\epsilon_0 R_c^3} \left[-Q_2 \mathbf{q}_1 - \frac{3Q_2}{R_c^2} ([Q_1] - \text{tr}([Q_1])) \mathbf{R}_c - \frac{3(\mathbf{R}_c \cdot \mathbf{q}_2)}{R_c^2} \mathbf{q}_1 \right] \quad (1.45)$$

The total force acting on body 2 is then:

$$\begin{aligned} \mathbf{F}_2 = \frac{1}{4\pi\epsilon_0 R_c^3} & \left[\left(Q_1 Q_2 - \frac{3Q_1}{R_c^2} \mathbf{R}_c \cdot \mathbf{q}_2 + \frac{3Q_2}{R_c^2} \mathbf{R}_c \cdot \mathbf{q}_1 + \frac{3Q_2}{2R_c^2} \text{tr}([Q_1]) + \frac{3Q_1}{2R_c^2} \text{tr}([Q_2]) \right. \right. \\ & + \frac{3}{R_c^2} \mathbf{q}_2 \cdot \mathbf{q}_1 - \frac{15Q_1[Q_2]}{2R_c^2} - \frac{15Q_2[Q_1]}{2R_c^2} - \frac{15}{2R_c^4} (\mathbf{R}_c \cdot \mathbf{q}_2) (\mathbf{R}_c \cdot \mathbf{q}_1) \left. \right) \mathbf{R}_c \\ & + Q_1 \mathbf{q}_2 + \frac{3Q_1}{R_c^2} ([Q_2] + \text{tr}([Q_2])) \mathbf{R}_c + \frac{3(\mathbf{R}_c \cdot \mathbf{q}_1)}{R_c^2} \mathbf{q}_2 - Q_2 \mathbf{q}_1 \\ & \left. - \frac{3Q_2}{R_c^2} ([Q_1] - \text{tr}([Q_1])) \mathbf{R}_c - \frac{3(\mathbf{R}_c \cdot \mathbf{q}_2)}{R_c^2} \mathbf{q}_1 \right] \quad (1.46) \end{aligned}$$

This can also be expressed in a table which allows for the easy ordering of terms. Dividing out the factor or $4\pi\epsilon_0 R_c^3$ yields Table 1.3

The terms are now ordered by which measures ($Q, \mathbf{q}, [Q]$) they incorporate. They are also ordered by their order in the dimensionless ratio r/R_c where r is a characteristic dimension of

either spacecraft. As the spacecraft move farther and farther away, the higher order terms in this variable matter less and less. The zeroth order term is in the upper left, the next diagonal contains the first order terms, and the next diagonal contains the second order terms. This table allows the selection of the force terms needed for appropriate fidelity.

As might be expected, the Force expression is symmetric, if one changes the sign on all \mathbf{R}_c terms and switches the indices the force on body 1 is found to be equal in magnitude but opposite in direction to the force on body 2. This satisfies Newton's 3rd law.

1.1.3.1.2 Torque derivation

The torque on body 2 can be found using a similar process. The torque is given by $\mathbf{T}_2 = \int_{B_1} \int_{B_2} \mathbf{r}_2 \times d\mathbf{F}$, where we can use the same binomial expansion as before to approximate $d\mathbf{F}$ to second order. this gives us:

$$\mathbf{T}_2 = \frac{1}{4\pi\epsilon_0 R_c^3} \int_{B_1} \int_{B_2} \mathbf{r}_2 \times (\mathbf{R}_c + \mathbf{r}_2 - \mathbf{r}_1) \left(1 - \frac{3r_1^2}{2R_c^2} - \frac{3r_2^2}{2R_c^2} - \frac{3(\mathbf{R}_c \cdot \mathbf{r}_2 - \mathbf{R}_c \cdot \mathbf{r}_1 - \mathbf{r}_2 \cdot \mathbf{r}_1)}{R_c^2} + \frac{15((\mathbf{R}_c \cdot \mathbf{r}_2)^2 + (\mathbf{R}_c \cdot \mathbf{r}_1)^2 - (\mathbf{R}_c \cdot \mathbf{r}_1)(\mathbf{R}_c \cdot \mathbf{r}_2))}{2R_c^4} \right) dq_2 dq_1 \quad (1.47)$$

Because of the extra \mathbf{r}_2 , many of the terms in the differential force expansion are now third order and can be neglected. The vector part of the differential force has three parts, one of which will be zero because $\mathbf{r}_2 \times \mathbf{r}_2 = 0$. The remaining terms can be grouped into two sets, those corresponding to the \mathbf{R}_c , and those with the \mathbf{r}_1 . The first one is evaluated below:

$$\mathbf{T}_{2_0} = \frac{1}{4\pi\epsilon_0 R_c^3} \int_{B_1} \int_{B_2} \mathbf{r}_2 \times \mathbf{R}_c \left(1 - \frac{3(\mathbf{R}_c \cdot \mathbf{r}_2 - \mathbf{R}_c \cdot \mathbf{r}_1)}{R_c^2} \right) dq_2 dq_1 \quad (1.48)$$

$$= -\frac{1}{4\pi\epsilon_0 R_c^3} \mathbf{R}_c \times \int_{B_1} \int_{B_2} \mathbf{r}_2 \left(1 - \frac{3(\mathbf{R}_c \cdot \mathbf{r}_2 - \mathbf{R}_c \cdot \mathbf{r}_1)}{R_c^2} \right) dq_2 dq_1 \quad (1.49)$$

Where higher order terms in the binomial expansion have been neglected. The integral is identical to the force integral for \mathbf{F}_{2_2} evaluated earlier, and can can be written down from inspection as:

$$\mathbf{T}_{2_0} = -\mathbf{R}_c \times \left[\frac{Q_1 \mathbf{q}_2}{R_c^3} + \frac{3(\mathbf{R}_c \cdot \mathbf{q}_1) \mathbf{q}_2}{R_c^5} + \frac{3Q_1 [Q_2] \mathbf{R}_c}{R_c^5} \right] \quad (1.50)$$

The other part of the torque comes from the \mathbf{r}_1 and is evaluated below:

$$\mathbf{T}_{2_1} = -\frac{1}{4\pi\epsilon_0 R_c^3} \int_{B_1} \int_{B_2} (\mathbf{r}_2 \times \mathbf{r}_1) dq_2 dq_1 \quad (1.51)$$

The binomial expansion here is truncated to just 1 because the $\mathbf{r}_2 \times \mathbf{r}_1$ term is already second order. This integral is completed as

$$\mathbf{T}_{2_1} = -\frac{1}{4\pi\epsilon_0 R_c^3} \mathbf{q}_2 \times \mathbf{q}_1 \quad (1.52)$$

The total torque is found by summing \mathbf{T}_{2_0} and \mathbf{T}_{2_1} and is given below:

$$\mathbf{T}_2 = \frac{1}{4\pi\epsilon_0 R_c^3} \left[Q_1 \mathbf{q}_2 \times \mathbf{R}_c + \frac{3(\mathbf{R}_c \cdot \mathbf{q}_1) \mathbf{q}_2 \times \mathbf{R}_c}{R_c^2} - \frac{3Q_1 \mathbf{R}_c \times [Q_2] \mathbf{R}_c}{R_c^2} + (\mathbf{q}_1 \times \mathbf{q}_2) \right] \quad (1.53)$$

Table 1.4: Torque ordering matrix

	Q_1	\mathbf{q}_1	$[Q_1]$
Q_2	0		
\mathbf{q}_2	$Q_1 \mathbf{q}_2 \times \mathbf{R}_c$	$\frac{3(\mathbf{R}_c \cdot \mathbf{q}_1) \mathbf{q}_2 \times \mathbf{R}_c}{R_c^2} + (\mathbf{q}_1 \times \mathbf{q}_2)$	
$[Q_2]$	$\frac{3Q_1 \mathbf{R}_c \times [Q_2] \mathbf{R}_c}{R_c^2}$		

This can be visualized in a table similar to the one for force. Once again dividing out the factor of $4\pi\epsilon_0 R_c^3$ leaves the torque ordering matrix shown in Table 1.4

As expected, there are no zeroth order terms, in fact there are no terms at all corresponding to the scalar charge Q_2 . Unlike the force expansion, the torque is not symmetric, i.e. $L_1 \neq -L_2$. This is because the torque on body 1 and body 2 are not measured about the same point, but rather the center of mass of each body. If all torques were measured about the same point, such as the barycenter of the system, the torques would be equal and opposite and would cancel out and not be able to change the angular momentum of the system.

1.1.3.2 Radial Field

In Reference 9, the force and torque on a charged body were found by assuming a differential force of

$$d\mathbf{F}_2 = \frac{Q_1 dq_2}{4\pi\epsilon_0 R^3} \mathbf{R} \quad (1.54)$$

and integrating over body 2. Rather than repeating this integration, The first column of the force and torque ordering tables can be used because they only consider the scalar charge of body 1. This yields

$$\mathbf{F}_2 = \frac{Q_1}{4\pi\epsilon_0 R_c^3} \left[Q_2 \mathbf{R}_c + \mathbf{q}_{\text{sep}} - \frac{3(\mathbf{q}_{\text{sep}} \cdot \mathbf{R}_c)}{R_c^2} \mathbf{R}_c + \frac{3[Q] \mathbf{R}_c}{R_c^2} + \frac{3\mathbf{R}_c}{2R_c^2} \text{trace}([Q]) - \frac{15}{2R_c^2} (\hat{\mathbf{e}}_r \cdot [Q] \hat{\mathbf{e}}_r) \mathbf{R}_c \right] \quad (1.55)$$

$$\mathbf{L}_2 = \frac{Q_1}{4\pi\epsilon_0 R_c^3} \left[\mathbf{q}_{\text{sep}} + \frac{3}{R_c^2} [Q] \mathbf{R}_c \right] \times \mathbf{R}_c \quad (1.56)$$

1.1.3.3 Flat Field

It is also of interest to calculate the force and torque on charged conducting bodies due to ambient fields. Although there can be small static electric fields at GEO or LEO, they are typically short lived and cannot change an orbit. The Lorentz field $\mathbf{v} \times \mathbf{B}$ however is sustained and much stronger. Any electric or Lorentz fields can be combined to form the total field $\mathbf{A} = \mathbf{E} + \mathbf{v} \times \mathbf{B}$. The velocity in this equation must be taken with respect to the earth's magnetic field, which co-rotates with earth. This means that a perfectly geostationary object will not feel this force. Although the strength and direction of the earth's magnetic field changes, the change across a small body like a spacecraft is negligible. Because of this locally flat assumption, the differential force is simply $d\mathbf{F} = \mathbf{A} dq$.

Because there is no spatial dependence to the differential force, the only measures that contribute to the force and torque are the scalar charge and the dipole.

The differential force on a differential charge moving at \mathbf{v} subject to \mathbf{E} and \mathbf{B} fields is given by:¹⁰

$$d\mathbf{F} = dq(\mathbf{E} + \mathbf{v} \times \mathbf{B}) \quad (1.57)$$

The torque about the center of mass on a body is defined as $\int_B \mathbf{r} \times d\mathbf{F}$, where \mathbf{r} points from the center of mass to the volume element. Using the differential force to find the force and torque on a body gives:

$$\mathbf{F} = \int_B (\mathbf{E} + \mathbf{v} \times \mathbf{B}) dq \quad (1.58)$$

$$\mathbf{L} = \int_B \mathbf{r} \times (\mathbf{E} + \mathbf{v} \times \mathbf{B}) dq \quad (1.59)$$

Since the fields do not change over the spacecraft body as shown in Figure 1.29, the terms \mathbf{E} and \mathbf{B} can be taken outside the integrals in Eqns. (1.58) and (1.59).

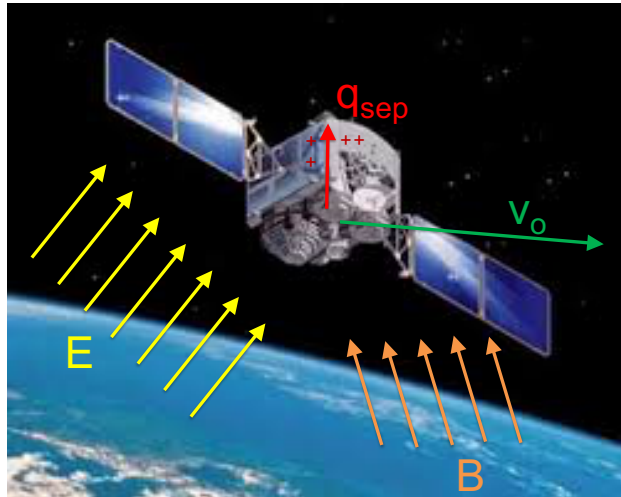


Figure 1.29: Flat \mathbf{E} and \mathbf{B} Field Configuration

1.1.3.3.1 Force Derivation:

To calculate the force experienced by a spacecraft in a flat field, the velocity variation over the body can be accounted for. The velocity is the orbital velocity \mathbf{v}_o plus the transport velocity: $\boldsymbol{\omega}_{B/\mathcal{E}} \times \mathbf{r}$,¹¹ where $\boldsymbol{\omega}_{B/\mathcal{E}}$ is the angular velocity between the satellite body frame \mathcal{B} and the magnetic field frame \mathcal{E} . Letting $\mathbf{v} = \mathbf{v}_o + \boldsymbol{\omega}_{B/\mathcal{E}} \times \mathbf{r}$ in Eq. (1.58):

$$\mathbf{F} = \mathbf{E} \int_B dq + \int_B (\mathbf{v}_o + \boldsymbol{\omega}_{B/\mathcal{E}} \times \mathbf{r}) \times \mathbf{B} dq \quad (1.60)$$

$$= \mathbf{E} \int_B dq - (\mathbf{B} \times \mathbf{v}_o) \int_B dq - \mathbf{B} \times \left(\boldsymbol{\omega}_{B/\mathcal{E}} \times \int_B \mathbf{r} \right) dq \quad (1.61)$$

$$= \mathbf{E} Q - (\mathbf{B} \times \mathbf{v}_o) Q - \mathbf{B} \times (\boldsymbol{\omega}_{B/\mathcal{E}} \times \mathbf{q}_{sep}) \quad (1.62)$$

Where the we have identified the total charge Q and defined the charge separation vector \mathbf{q}_{sep} as a generalization of the dipole moment.¹⁰

$$Q = \int \rho dV \quad \text{and} \quad \mathbf{q}_{\text{sep}} = \int \mathbf{r} \rho dV \quad (1.63)$$

In many scenarios the orbital velocity \mathbf{v}_o , even taken in the ECEF frame, will dwarf the transport velocity $\boldsymbol{\omega}_{\mathcal{B}/\mathcal{E}} \times \mathbf{r}$. For a spacecraft with $r = 1$ m, $\boldsymbol{\omega}_{\mathcal{B}/\mathcal{E}} = 1$ deg/sec, and an ECEF orbital velocity of 1 km/sec, the ratio of the transport velocity to the orbital velocity will be less than 10^{-5} . In many scenarios the transport term can be dropped leaving:

$$\mathbf{F} = (\mathbf{E} + \mathbf{v}_o \times \mathbf{B}) Q \quad (1.64)$$

1.1.3.3.2 Torque Derivation:

Substituting the transport velocity expression into Eq. (1.59) and carrying through a triple product expansion and one cancellation the torque is found to be:

$$\mathbf{L} = -(\mathbf{E} + \mathbf{v}_o \times \mathbf{B}) \times \mathbf{q}_{\text{sep}} + \boldsymbol{\omega}_{\mathcal{B}/\mathcal{E}} \times \int_{\mathcal{B}} (\mathbf{B} \cdot \mathbf{r}) \mathbf{r} dq \quad (1.65)$$

$$= -(\mathbf{E} + \mathbf{v}_o \times \mathbf{B}) \times \mathbf{q}_{\text{sep}} + B \boldsymbol{\omega}_{\mathcal{B}/\mathcal{E}} \times \int_{\mathcal{B}} (r^2 \cos(\theta)) \hat{\mathbf{r}} dq \quad (1.66)$$

Where θ is defined as the angle between \mathbf{r} and \mathbf{B} . Much like a pendulum experiences a torque that aligns an offset mass with a gravity field, the first term describes a torque that aligns the dipole moment \mathbf{q}_{sep} with $\mathbf{E} + \mathbf{v}_o \times \mathbf{B}$. The second term provides a torque perpendicular to both the rotation and the magnetic field, and quadratically proportional to the charge separation. This term will only be significant when \mathbf{v}_o is comparable to $r\boldsymbol{\omega}_{\mathcal{B}/\mathcal{E}}$, which will only happen at extremely fast spin rates. If we neglect this term, the torque is given by:

$$\mathbf{L} = -(\mathbf{E} + \mathbf{v}_o \times \mathbf{B}) \times \mathbf{q}_{\text{sep}} \quad (1.67)$$

This is the exact answer for the torque on a dipole in a flat field, and is found in multiple undergraduate physics texts.^{10,12}

1.1.3.3.3 MSM and AFM equivalency in flat fields

In Reference 13, the force and torque experienced by a charged object in a flat field is given by:

$$\mathbf{F} = \sum_i^N q_i \mathbf{A} = \mathbf{A} \sum_i^N q_i = \mathbf{A} Q \quad (1.68)$$

This is the same result as was found using AFMs. This is because the fields do not change over the body. Likewise the torque is given by

$$\mathbf{L} = \sum_i^N \mathbf{r}_i \times \mathbf{A} q_i = -\mathbf{A} \times \sum_i^N \mathbf{r}_i q_i \quad (1.69)$$

Noticing the dipole $\mathbf{q}_{\text{sep}} = \int_b \mathbf{r} dq = \sum_i^N \mathbf{r}_i q_i$ gives

$$\mathbf{L} = -\mathbf{A} \times \mathbf{q}_{\text{sep}} \quad (1.70)$$

Once again, this result is equivalent to the AFM answer. This is only true because the differential forces does not vary through-out the body, and no truncated binomial expansion is needed to approximate it.

While the numerical solution form of AFM and MSM in a flat force fields are equivalent, the parameters for each model are arrived at differently. The MSM parameters are obtained through an optimization process to fit it to expected E-forces about a general body, while the AFM parameters are obtained from the expansion terms of the E-field. The AFM process has not fitting or tuning, which is a benefit. However, the MSM performance can be better as the parameters can be tuned to approximate a local E-force behavior.

1.1.3.4 Predictive AFMs

The AFM process has two steps. The first is to derive certain measures useful for predicting the electrostatic force and torque. This has been done above and it is seen that predicting force and torque with the accuracy below 5% is very possible for separations of less than 50 meters. The second part is to predict those measures using the voltage of each craft and their separation. These variables would be much easier to measure in an actual mission than the charge distribution.

The influence of an ambient field and the voltage of both craft on the zeroth, first, and second order term is shown in the table below:

Table 1.5: *AFM prediction*

	\mathbf{A}_a	V_t	V_d
Q		C_S	C_M
\mathbf{q}_{sep}	$[\chi_a]$	χ_S	χ_M
$[Q]$	$[\psi_a(\mathbf{A}_a)]$	$[\psi_S]$	$[\psi_M]$

Where $\mathbf{A} = \mathbf{E} + \mathbf{v} \times \mathbf{B}$. In this table the moments of the charge distribution are listed on the left-most column, and the effect that perturbs it is shown in the top row. The subscripts stand for Ambient, Self, and Mutual. C is the capacitance, ψ captures the effect on the charge tensor, and χ captures the effect on dipole. The susceptibilities will be derived for both a inter-craft and flat field situation

1.1.3.4.1 Inter-Craft predictive AFMs

If two conductors with n_1 and n_2 spheres each are considered, the PDC matrix can be put into block form:

$$\begin{bmatrix} \mathbf{V}_1 \\ \mathbf{V}_2 \end{bmatrix} = \frac{1}{4\pi\epsilon_0} \begin{bmatrix} C_{i1} & C_{iM} \\ C_{iM}^T & C_{i2} \end{bmatrix} \begin{bmatrix} \mathbf{q}_1 \\ \mathbf{q}_2 \end{bmatrix} \quad (1.71)$$

Where the voltage and charge of each craft have been separated. Note that the self capacitance terms C_{i1} and C_{i2} are much larger than the mutual capacitance term C_{iM} because the inter-sphere separations are much smaller inside one body rather than between the two bodies. Additionally, the self capacitance matrices contain the diagonal $1/R$ terms which are larger than the off-diagonal $1/r$ terms.

As an example, consider two oblong bodies with effective diameter of 1 meter and SMSM sphere radius of 0.1 meters separated by 10 meters. The self capacitance matrices will be full of

terms ranging in size from $1/R = 1/0.1 = 10$ to $1/r = 1/1 = 1$. The mutual capacitance matrix will be full of terms $1/(R - 2r) = 1/(10 - 2) = 1/8$ to $1/(R + 2r) = 1/(10 + 2) = 1/12$.

To find the charges, from which the forces and torques can be computed, this matrix can be computed using the block diagonal psuedoinverse with a simplification for the symetry.

$$\begin{bmatrix} A & B \\ B^T & D \end{bmatrix}^{-1} = \begin{bmatrix} (A - BD^{-1}B^T)^{-1} & -A^{-1}B(D - B^T A^{-1}B)^{-1} \\ -D^{-1}B^T(A - BD^{-1}C)^{-1} & (D - B^T A^{-1}B)^{-1} \end{bmatrix} \quad (1.72)$$

Recognizing that A and D represent the self capacitance matrices, which contain much larger terms than the mutual matrix B , terms second order in B are dropped:

$$\begin{bmatrix} A & B \\ B^T & D \end{bmatrix}^{-1} \approx \begin{bmatrix} A^{-1} & -A^{-1}BD^{-1} \\ -D^{-1}B^T A^{-1} & D^{-1} \end{bmatrix} = \begin{bmatrix} C_1 & -C_1 C_{iM} C_2 \\ -C_2 C_{iM}^T C_1 & C_2 \end{bmatrix} \quad (1.73)$$

The two matrices C_1 and C_2 are not functions of the state consisting of relative separation and orientation. Notice that the inverse of the mutual capacitance matrix does not need to be taken, but it is a function of the state. The terms in C_{iM} are of the form

$$[C_{iM}]_{i,j} = \frac{1}{4\pi\epsilon_0 \|\mathbf{R}_c + \mathbf{r}_{2_i} - \mathbf{r}_{1_j}\|} \quad (1.74)$$

Hidden in this equation is the dependance on relative state. Although \mathbf{r}_1 and \mathbf{r}_2 do not change in the body fixed frame of their respective craft, DCMs need to be used to ensure all three vectors are in the same frame. However, since the center to center separation R_c is much greater than the dimensions of either craft r_1 or r_2 , this can be approximated as

$$[C_{iM}]_{i,j} = \frac{1}{4\pi\epsilon_0 \|\mathbf{R}_c + \mathbf{r}_{2_i} - \mathbf{r}_{1_j}\|} \sim \frac{1}{4\pi\epsilon_0 R_c} \quad (1.75)$$

Approximating all elements in the mutual capacitance matrix as $1/R_c$ allows the relative state to be ignored while still capturing some first-order mutual capacitance and susceptibility. The inverse capacitance matrix can now be approximately inverted as

$$\begin{bmatrix} \mathbf{q}_1 \\ \mathbf{q}_2 \end{bmatrix} = \frac{1}{4\pi\epsilon_0} \begin{bmatrix} C_1 & -C_1 \mathbb{1}(n_1, n_2) C_2 / (4\pi\epsilon_0 R_c) \\ -C_2 \mathbb{1}(n_2, n_1) C_1 / (4\pi\epsilon_0 R_c) & C_2 \end{bmatrix} \begin{bmatrix} \mathbf{V}_1 \\ \mathbf{V}_2 \end{bmatrix} \quad (1.76)$$

If the two bodies are both conductors and each MSM sphere is at the same voltage this matrix equation can be transformed to a vector equation

$$\mathbf{q}_1 = [C_1] \mathbb{1}(n_1, 1) V_1 - \frac{[C_1] \mathbb{1}(n_1, n_2) [C_2]}{4\pi\epsilon_0 R_c} \mathbb{1}(n_2, 1) V_2 \quad (1.77)$$

$$\mathbf{q}_2 = [C_2] \mathbb{1}(n_2, 1) V_2 - \frac{[C_2] \mathbb{1}(n_2, n_1) [C_1]}{4\pi\epsilon_0 R_c} \mathbb{1}(n_1, 1) V_1 \quad (1.78)$$

Now that the charge on each MSM sphere is approximated as a function of a collection of matrices that do not change with state and the scalar voltage of each craft, the susceptibility of the scalar charge, dipole, and charge tensor can be found.

1.1.3.4.1.1 Susceptibility of the Scalar Charge

The effect of a nearby charged object on the voltage-to-charge relationship is widely known as mutual capacitance, but will be referred to here as susceptibility to match the higher order terms. The total charge is found by summing the charge on each sphere

$$Q = \sum \mathbf{q} = \mathbb{1}(1, n) \mathbf{q} \quad (1.79)$$

Thus, the scalar charge of body 1 is given by

$$Q_1 = C_S V_1 + C_M V_2 \quad (1.80)$$

Where the self and mutual capacitances are given by

$$C_S = \mathbb{1}(1, n_1) [C_1] \mathbb{1}(n_1, 1) = \sum \sum [C_1] \quad (1.81)$$

$$C_M = \frac{-\mathbb{1}(1, n_2) [C_1] \mathbb{1}(n_1, n_2) [C_2] \mathbb{1}(n_2, 1)}{4\pi\epsilon_0 R_c} = \frac{\sum \sum [C_1] \mathbb{1}(n_1, n_2) [C_2]}{4\pi\epsilon_0 R_c} \quad (1.82)$$

The scalar self capacitance can be computed with high fidelity using a SMSM model with hundreds or thousands of spheres and re-used in each time step for computation. The numerator of the mutual capacitance can be similarly computed at high fidelity and then divided by the scalar separation vector at each time step.

1.1.3.4.1.2 Susceptibility of the Dipole

The dipole \mathbf{q}_{sep} is defined in a continuous charge distribution and MSM model as

$$\mathbf{q}_{\text{sep}} = \int_B \mathbf{r} dq = \sum_i^N \mathbf{r}_i q_i = [R] \mathbf{q} \quad (1.83)$$

where $[R]$ is a $3 \times N$ matrix containing the x , y , and z coordinates of each MSM sphere:

$$[R] = \begin{bmatrix} x_1 & \dots & x_N \\ y_1 & \dots & y_N \\ z_1 & \dots & z_N \end{bmatrix} \quad (1.84)$$

The dipole can now be written as a function of the voltages of both craft using the letter χ

$$\mathbf{q}_{\text{sep}} = \chi_S V_1 + \chi_M V_2 \quad (1.85)$$

Where the self and mutual susceptibilities of the dipole for body 1 are

$$\chi_S = [R_1] [C_1] \mathbb{1}(n_1, 1) \quad (1.86)$$

$$\chi_M = \frac{-[R_1] [C_1] \mathbb{1}(n_1, n_2) [C_2] \mathbb{1}(n_2, 1)}{4\pi\epsilon_0 R_c} \quad (1.87)$$

Once again, these 3×1 vectors can be computed with high fidelity from SMSM models of each body. Each element in the mutual term must be divided by the separation distance which may change with time.

1.1.3.4.1.3 Susceptibility of the Charge Tensor

The charge tensor is defined from a continuous charge distribution or MSM model as

$$[Q] = \int_B -[\tilde{\mathbf{r}}][\tilde{\mathbf{r}}]d\mathbf{q} = \sum_i^N -[\tilde{\mathbf{r}}_i][\tilde{\mathbf{r}}_i]q_i = -[R_s][A]\mathbf{q} \quad (1.88)$$

where $[R_s]$ is a $3 \times 3N$ matrix containing the double cross product matrix of each MSM sphere position and A is a $3N \times N$ matrix used to interweave three copies of the charge vector made from the small vector a .

$$[R_s] = \begin{bmatrix} [\tilde{\mathbf{r}}_1][\tilde{\mathbf{r}}_1] \\ \vdots \\ [\tilde{\mathbf{r}}_N][\tilde{\mathbf{r}}_N] \end{bmatrix} \quad [a] = \begin{bmatrix} 1 \\ 1 \\ 1 \end{bmatrix} \quad [A] = \begin{bmatrix} a & 0 & \dots & 0 \\ 0 & a & \dots & 0 \\ \vdots & \vdots & \ddots & \vdots \\ 0 & 0 & \dots & a \end{bmatrix} \quad (1.89)$$

The charge tensor is now found as a function of both voltages, and two 3×3 matrices,

$$[Q_1] = [\psi_S]V_1 + [\psi_M]V_2 \quad (1.90)$$

where the self and mutual susceptibilities of the charge tensor for body 1 are given by

$$[\psi_S] = -[R_{s_1}][A][C_1]\mathbb{1}(n_1, 1) \quad (1.91)$$

$$[\psi_M] = [R_{s_1}][A] \frac{[C_1]\mathbb{1}(n_1, n_2)[C_2]\mathbb{1}(n_2, 1)}{4\pi\epsilon_0 R_c} \quad (1.92)$$

These matrices can be found using high fidelity SMSM models before propagation and the mutual term can be adjusted by the separation distance. The derivations have been done for body 1, but body 2 can easily be found by adjusting subscripts.

1.1.3.4.2 Flat Field Susceptibilities

In a flat field the only Measures that contribute to force or torque are the scalar charge and the dipole. An object's self capacitance relates its voltage to its scalar charge, and the ambient field has no effect. The ambient field does have an effect on the dipole however. The dipole can be thought of as the total charge Q multiplied by the separation of the center of charge from the center of mass. If the voltage increases, so will the charge which increases the magnitude of the dipole, but not the direction. An ambient field will push all the charge to one end of the spacecraft. How far an ambient field is able to move the center of charge is dependent on the geometry and attitude of the spacecraft with respect to the ambient field. These two effects can be lumped into the following equation:

$$\mathbf{q}_{\text{sep}} = \chi_S V + [\chi_A]\mathbf{A} \quad (1.93)$$

Both of these susceptibilities (χ_S and $[\chi_A]$) can be found empirically by recording the charge distribution at different voltages and ambient fields, or from a MSM model. In this analysis a Surface MSM (SMSM) model with a hundred spheres is used to generate the susceptibilities. If

$[R]$ contains the positions of all MSM spheres from the center of mass, and q is a vector of the charges on each sphere the dipole can be formed as:

$$[R] = \begin{bmatrix} x_1 & y_1 & z_1 \\ \vdots & \vdots & \vdots \\ x_N & y_N & z_N \end{bmatrix} \quad (1.94)$$

$$\mathbf{q}_{\text{sep}} = [R]^T \mathbf{q} \quad (1.95)$$

$$(1.96)$$

using the capacitance relation to find the charges gives

$$\mathbf{q}_{\text{sep}} = [R]^T ([C]\mathbf{V} + [C][R]\mathbf{A}) \quad (1.97)$$

$$\mathbf{q}_{\text{sep}} = \chi_S \mathbf{V} + [\chi_A]\mathbf{A} \quad (1.98)$$

Where these new parameters are defined below:

$$\chi_S = [R]^T [C] \mathbf{1}(N, 1) \quad (1.99)$$

$$[\chi_A] = [R]^T [C] [R] \quad (1.100)$$

Putting all of the together the force and torque on a charged conductor is given by

$$\mathbf{F} = C_S \mathbf{V} \mathbf{A} \quad (1.101)$$

$$\mathbf{L} = (\chi_S \mathbf{V} + [\chi_A]\mathbf{A}) \times \mathbf{A} \quad (1.102)$$

χ_S and $[\chi_A]$ are constants in the body frame. Direction Cosine matrices are needed to rotate \mathbf{A} into the body frame to compute torque.

1.1.3.5 Inter-Craft Analysis

Terms that are low order in r/R_c will dominate, especially as the craft move apart. However there are some situations when higher order terms can contribute more than low order terms. Consider calculating the torque on a very geometrically simple object such as a cylinder or cube with the center of mass assumed to be at the center of the volume.

The torque on the object in the presence of a point charge is given by:

$$\mathbf{L}_2 = \frac{Q_1}{4\pi\epsilon_0 R_c^3} \left[\mathbf{q}_{\text{sep}} + \frac{3}{R_c^2} [Q] \mathbf{R}_c \right] \times \mathbf{R}_c \quad (1.103)$$

re-writing this in terms of susceptibilities gives:

$$\mathbf{L}_2 = \frac{C_{S1}V_1 + C_MV_2}{4\pi\epsilon_0 R_c^3} \left[(\chi_S V_2 + \chi_M V_1) + \frac{3}{R_c^2} ([\psi_S]V_2 + [\psi_M]V_1) \mathbf{R}_c \right] \times \mathbf{R}_c \quad (1.104)$$

$$= \frac{C_{S1}V_1 + C_MV_2}{4\pi\epsilon_0 R_c^3} \left[\chi_S V_2 + (\chi_M V_1 + \frac{3}{R_c^2} [\psi_S] \mathbf{R}_c V_2) + \frac{3}{R_c^2} [\psi_M] \mathbf{R}_c V_1 \right] \times \mathbf{R}_c \quad (1.105)$$

where the terms have been re-grouped by order. It would seem that the dipole terms should dominate. However, if the center of volume of a conducting body is also the same as the center of mass, symmetric matrices left multiplied by $[R_2]$ will be zero. This makes χ_S and χ_M equal to zero. So for symmetric bodies, it is actually the second order term associated with the charge tensor $[\psi_S]$ that dominates.

As an example of this case, consider a cylinder and point charge in the X-Y plane as is shown in Figure 1.2. The lowest order torque is:

$$L_2 = \frac{C_{S1}V_1 + C_MV_2}{4\pi\epsilon_0R_c^3} \left[\frac{3}{R_c^2} [\psi_S] \mathbf{R}_c V_2 \right] \times \mathbf{R}_c = A \mathbf{R}_c \times [\psi_S] \mathbf{R}_c \quad (1.106)$$

where constants have been lumped into A . Assume the point charge is at a constant distance but moves in a circle around the cylinder. \mathbf{R}_c is then given by

$$\mathbf{R}_c = \begin{bmatrix} R \cos(\theta) \\ R \sin(\theta) \\ 0 \end{bmatrix} \quad (1.107)$$

$[\psi_S]$ is constant and diagonal in the body frame and the torque will only be about the z axis. It is of the form

$$L_z \propto \cos(\theta) \sin(\theta) = \frac{1}{2} \sin(2\theta) \quad (1.108)$$

This angular dependance was found by Stevenson (Citation), but was curve fit rather than derived.

Many actual spacecraft will have at least a little offset between their center of charge and center of mass, and it does not take more than a few centimeters of offset to overpower the second order term depending on voltages and separation. A very un-symmetric spacecraft such as the box and wing model used earlier has an offset of nearly a meter. If only this term is kept the torque is given by

$$L_2 = \frac{C_{S1}V_1 + C_MV_2}{4\pi\epsilon_0R_c^3} \left[\chi_S V_2 \right] \times \mathbf{R}_c = A \chi_S \times \mathbf{R}_c \quad (1.109)$$

where the constants have one again been lumped into A . If the center of mass offset is in the plane of the point charge, the torque will still be about the z axis and is of the form:

$$L_z \propto \cos(\theta + \phi) \quad (1.110)$$

Where ϕ allows for the phase to shift depending on the CM offset. As one can see, Eqns. (1.110) and (1.108) will predict different torques, and in two quadrants they will even predict torques of different signs. Knowledge of center of mass to center of charge differences are essential for the stability of control laws used for de-spinning of passive space debris.

1.1.3.6 Flat field Analysis

Space situational awareness (SSA) requires high-fidelity models to predict the positions of objects in orbit. Some objects are especially sensitive to non-gravitational perturbations and are called High Area-to-Mass Ratio (HAMR) objects. This class of objects was first noticed by Schildknecht.¹⁴ Especially at Geosynchronous (GEO) altitudes, Solar Radiation Pressure (SRP) significantly drives the orbit. SRP depends on the attitude of the object, which demands that attitude be taken into account when propagating these objects.

Although SRP is the largest non-gravitational perturbation, it may not be sufficient to explain the motions of all HAMR objects. Wiesel¹⁵ recently reported some objects which appear to accelerate *towards* the sun during the propagation interval. This paper adds electrostatic and eddy-current torques to the non-gravitational perturbations used for propagation of HAMR objects at GEO. Freuh was the first to consider electric effects on HAMR objects.¹⁶

Many of these HAMR objects are thought to be ripped pieces of Multi-Layer Insulation (MLI).¹⁷ Samples returned from the Hubble Space Telescope had a tendency to curl up when peeling off.¹⁸ Objects in GEO, such as ripped or fragmented MLI, can charge to very high levels (such as 10s of kilo-Volts in the Earth's shadow).¹⁹ This charge will feel the Loentz force ($\mathbf{F} = q\mathbf{v} \times \mathbf{B}$) which can affect the object's orbit or attitude in a small way. This small change can couple to stronger perturbations such as SRP to create large orbital changes.

This section investigates the sensitivity of HAMR orbits to electrostatic perturbations by developing novel rapid methods for electrostatic force and torque prediction in a locally flat environmental magnetic field. Novel models for eddy torques are also used, and other standard perturbations (earth spherical gravity, sun and moon gravity, SRP, and gravity gradients) are also used. Although the change in orbital elements due to electrostatics alone is small, it can "steer" larger perturbations like SRP to create drastic differences after only 12 hours of propagation time.

To study this, orbits are numerically propagated with and without charging effects taken into account. The electrostatic force and torque have already been presented, and the eddy torque is described below.

1.1.3.6.1 Eddy Current Torque

When a conductor spins in a magnetic field, the mobile electrons move in loops because of induction. No net force is felt because the current travels in a closed loop, but a torque is felt. Gomez recently developed a general method for calculating this torque²⁰ which is summarized here.

$$\mathbf{L} = ([M](\boldsymbol{\omega} \times \mathbf{B})) \times \mathbf{B} \quad (1.111)$$

For a flat plate, $[M]$ is given by

$$[M] = C_T \frac{\sigma e}{4} \mathbf{n} \mathbf{n}^T \quad (1.112)$$

Where σ is the conductivity, C_T is a constant dependent on shape and size, and \mathbf{n} is a unit vector normal to the plane. For a rectangle with length l greater than width w , C_T is given by

$$C_T = \frac{lw^3}{3(1 + 1.38(\frac{w^2}{l^2})^{1.36})} \quad (1.113)$$

in the cases considered here the normal axis is \hat{z} which makes the torque equal to

$$\mathbf{L} = ([M](\boldsymbol{\omega} \times \mathbf{B})) \times \mathbf{B} = C_T \frac{\sigma e}{4} (\omega_1 B_2 - \omega_2 B_1) \begin{bmatrix} B_2 \\ B_1 \\ 0 \end{bmatrix} \quad (1.114)$$

It is interesting to note that if the plate is spinning about it's axis of maximum inertia, ω_3 will be large and $\omega_1 \omega_2$ will be small or zero. The eddy torque will then be zero, and there is no way to remove that last bit of spin about the axis of major inertia. This indicates that very thin objects will spin down in all axes but one if only eddy torques are considered.

1.1.3.6.2 Analytical Bounding Cases

Before numerical analysis, it is prudent to bound the effects that charging could have on an orbit. Consider a thin (1/4 mil) sheet of aluminized mylar one square meter in size. The self capacitance of this object will be near 40 pF, assuming a voltage of 30 kV gives a total charge of

1.2 μC . There is no sustained electric field at GEO, but the orbital velocity combines with earth's magnetic field to create a Lorentz force $\mathbf{F} = q\mathbf{v} \times \mathbf{B}$. The velocity must be with respect to the magnetic field, which co-rotates with earth. Therefore, a perfectly geostationary object, no matter how charged, will feel no force. However, many uncontrolled GEO objects get pulled up to higher inclinations $\sim 16^\circ$ by the moon's gravity.²¹ This gives a velocity with respect to the magnetic field of $v = v_o \sin(i) = 3.075 \frac{\text{km}}{\text{s}} \sin(16^\circ) \approx 1 \text{ km/s}$. The \mathbf{B} -field at GEO is near 100 nT, which gives an effective \mathbf{E} field of 100 $\mu\text{N/m}$. Combining this effective electric field with the charge gives an upper bound of $1.2 * 10^{-10}\text{N}$ for this object. The sheet only weighs 8.8 grams, but the acceleration due to charging only causes an acceleration of $1.36 * 10^{-8} \text{ m/s}^2$.

As a comparison, the upper bound for SRP is given by $F = PA = 4.57 * 10^{-6} \times 1 \text{ N}$ and an acceleration of $5.177 * 10^{-4} \text{ m/s}^2$. SRP is clearly the stronger force by nearly 5 orders of magnitude. The change in the Keplerian orbital elements will now be investigated. The force from charging must act perpendicularly to both the relative velocity and the magnetic field, however in this analysis we assume it acts in the velocity direction to simplify analysis. Using Gauss' variational equations of motion to calculate the perturbative effect gives the change in semi-major axis (SMA) over one day gives

$$\frac{da}{dt} \Delta t = \frac{2a_s}{n} (1 \text{ day}) \approx 32 \text{ meters} \quad (1.115)$$

Whereas the change in SMA over a day from SRP is 1,230 km. It would seem that electrostatic effects are negligible, however, since SRP is very sensitive to the attitude of the plate, small electrostatic forces and torques can influence the large forces from SRP. This can create large (100s of km) differences after an orbit.

1.1.3.6.3 Numerical Analysis of Orbit

Many perturbations influence the orbits of HAMR objects at GEO. Each perturbation considered is detailed in Tab. 1.6 with either the exact equation or a short description.

Table 1.6: Forces and Torques acting on Space Debris

Perturbation	Force	Torque
Earth gravity	Spherical Harmonics up to 4th order	$\mathbf{L} = \frac{3\mu}{R_c^3} \mathbf{R}_c \times [I] \mathbf{R}_c$
Lunar gravity	point-mass gravity	0
Solar gravity	point-mass gravity	0
SRP	Absorptive, specular, and diffuse reflection	$\mathbf{L} = \mathbf{r}_{\text{sep}} \times \mathbf{F}_{\text{SRP}}$
Electrostatic	$\mathbf{F} = Q\mathbf{v} \times \mathbf{B}$	$\mathbf{L} = \mathbf{q}_{\text{sep}} \times (\mathbf{v} \times \mathbf{B})$
Eddy Currents	0	$\mathbf{L} = ([M](\boldsymbol{\omega} \times \mathbf{B})) \times \mathbf{B}$

The magnitude of the SRP force is determined by the solar flux and the illuminated area. The direction is governed by the amount of light that is absorbed and reflected specularly and diffusely. The SRP force is given by:²²

$$\mathbf{F} = p_{\text{SRP}} A \cos(\theta) \left[\rho_A \hat{\mathbf{s}} + 2\rho_S \cos(\theta) \hat{\mathbf{n}} + \rho_D \left(\hat{\mathbf{s}} + \frac{2}{3} \hat{\mathbf{n}} \right) \right] \quad (1.116)$$

Where θ is the angle between the sun-pointing line and the face normal, $\hat{\mathbf{s}}$ is the sun-pointing vector, $\hat{\mathbf{n}}$ is normal to the plane, and ρ_A , ρ_S , and ρ_D are the absorptive, specular, and diffuse coefficients, respectively, which must sum to unity.

The electrostatic perturbations depend on three constants C_s , χ_S and $[\chi_A]$, which are used to translate the voltage and ambient field to the charge and dipole. These parameters are found as functions of plate sizes below.

1.1.3.6.3.1 Self Capacitance Estimation

Calculating the self capacitance of a square plate is a long-studied problem. J.C. Maxwell himself estimated it for a 1 cm square to be 0.40 pF,²³ and current computation methods now estimate it at 0.4019 pF.²⁴ The self capacitance to two geometrically similar objects, will scale linearly with any dimension. For instance, the self capacitance of a sphere is given by $C = 4\pi\epsilon_0 R$. For a flat plate, capacitance can be expressed as $c = C/B$ where C is the true capacitance in Farads, and B is the bigger side of the plate. For a square plate B is just the edge length.

Reitan and Higgins produced a very useful curve from which can be extrapolated c from the aspect ratio of the big to small side B/S .²⁵ Ten points are read off this curve, and a power law is used to fit it with good accuracy ($r^2 = 0.9995$). The power law is shown below.

$$c = \left(0.402 * 10^{-10} \frac{\text{F}}{\text{m}}\right) \left(\frac{B}{S}\right)^{-0.4733} \quad (1.117)$$

The capacitance is used to convert the voltage, which can often be estimated from space weather parameters and is assumed to not depend on size or shape, to the charge. The amount of charge will dictate the magnitude of the force.

The capacitance grows linearly with size, the area grows quadratically, and the mass grows cubically. This means that the acceleration due to an area-based perturbation such as SRP will go like $1/r$ while the acceleration from charging-based perturbations will go like $1/r^2$. This means charging will be most significant for small objects. Small objects are also the hardest to track from earth, but may still pose collision risks to GEO satellites.

1.1.3.6.3.2 AFM parameter estimation through SMSM

Once the self capacitance is known, the AFM parameters χ_S and $[\chi_A]$ must be estimated. There are many ways to estimate these parameters, the method used in this analysis is to generate a SMSM mesh for the chosen shape and compute the AFM parameters from the positions and sizes of the spheres as is shown in Eq. (1.99) and (1.100). The MSM model is created by dividing the plate into N small squares of side length $dx = \sqrt{BS/N}$ and placing a sphere at each node in the mesh. This sets three of the four free parameters associated with each sphere. The radii of all spheres is varied until the self capacitance of the MSM model is equivalent to the self capacitance of the plate computed from the empirical power law. Then each sphere is shifted by r_{sep} to account for the center of mass to center of area difference. Finally, Eq. (1.99) and (1.100) are used to compute χ_S and $[\chi_A]$.

The completed MSM model with correctly sized spheres and color indicating the charge on each sphere when charged to 30 kV is shown in Fig. 1.30. As one can see, more charge (shown as color) accumulates near the corners of the plate. The center of charge is located in the center of area, but the center of mass, about which torques are taken, is removed by 2 mm in \hat{x} and \hat{y} . The center of charge will also move due to the Lorentz field, although this effect is small compared to the center of mass offset of 2.82 mm. For example, this 10 cm plate charged to 30 kV in a Lorentz field created from a velocity of 1 km/s orthogonal to a 100 nT magnetic field will only see a charge-center move of 7.7 pm. The torque produced by the center of mass offset is a much stronger

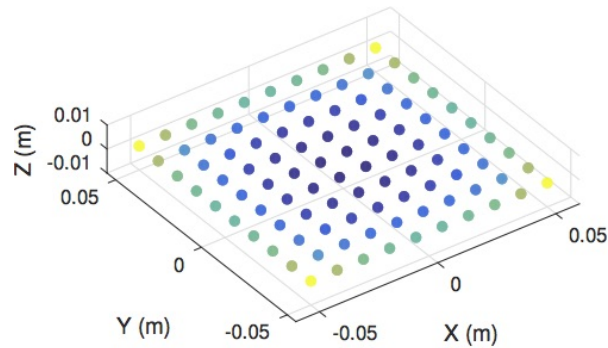


Figure 1.30: Flat plate modeled with SMSM, color indicates charge

(more than 8 orders of magnitude) than the torque created by the induced effect. Nonetheless, both effects are included.

Since χ_S is the dominant term, it is prudent to note that it can also be computed as $\chi_S = C r_{\text{sep}}$ where C is the capacitance in Farads and r_{sep} is a vector that points from the center of mass to the center of charge. This can be combined with Eq. (1.117) to yield the dominant electrostatic terms for a rigid plate.

1.1.3.6.3.3 Magnetic Field and Charging Models

Earth's magnetic field can be approximated as an inclined dipole for simple calculations. For more accurate calculations close to earth the IGRF model can be used, which takes many factors affecting earth's geodynamo into account. Outside Earth's magnetosphere, the magnetic is purely a function of space weather and has little to no dependence on earth's own magnetic field. At GEO, these two effects combine to make a complex function of time and space weather parameters. The current state of the art for modeling this field is the Tsyganenko model.²⁶ There have been many versions and updates to this model in this analysis the 2001 version is used with GEOPACK 2008.¹

This model has been implemented and is run at each timestep. The time is assumed to be January 1, 2002, midnight, for all runs. The space weather parameters used are representative, and are the same as is used by the Community Coordinated Modeling Center (CCMC) on their single-run website², and are summarized in Table 1.7.

Table 1.7: Space weather parameters used for Tsyganenko model

Parameter	Value
Solar Wind Dynamic Pressure	4 nPa
Solar Wind Velocity	400 km/s
IMF B_y	6 nT
IMF B_z	-5 nT
DST	-30 nT

¹<http://ccmc.gsfc.nasa.gov/modelweb/magnetos/tsygan.html>

²<http://ccmc.gsfc.nasa.gov/requests/instant/tsyganenko.php>

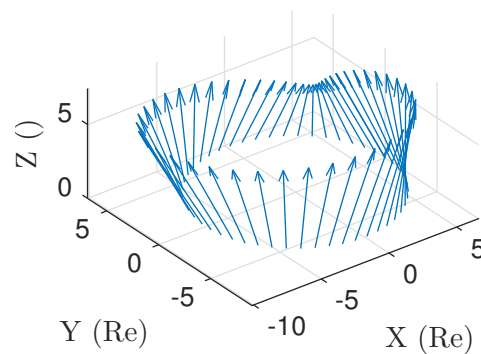


Figure 1.31: ECI Magnetic field used in this study, Z axis is arbitrary

This produces a magnetic field that is deformed by the solar wind. As shown in Fig. 1.31, the field does not look like a tilted dipole.

The voltage of a conducting sheet is perhaps one of the easier spacecraft charging problems one could pose, nonetheless it is still a hard problem. The voltage was modeled under very harsh charging conditions using NASCAP 2K in by Früh²⁷ for a sheet with one side conducting and one of different dielectrics such as Kapton and Mylar. The highest voltage found was slightly more than -30 kV and occurred when using the ATS-6 flux. In this analysis a simple and constant value of -30 kV is used to give a rough maximum for the charge level. In many circumstances, the voltage would be much smaller.

1.1.3.6.3.4 Nominal Numerical Propagation

A nominal case of a thin rigid square of MLI is considered. The material parameters are shown in Tab. 1.8. Any matrix values not explicitly defined are zero.

Table 1.8: Nominal HAMR propagation values^{16,28}

Parameter	Value
thickness	1/4 mil
density	1.39 g/cm ³
L_x	10 cm
L_y	10 cm
C	4.02 pF
\mathbf{r}_{sep}	$[2, 2, 0]^T$ mm
χ_S	$8.043 * [1, 1, 0]^T$ fF m
$\psi_A(1, 1)$	$5.393 * 10^{-11}$ F m ²
$\psi_A(2, 1), \psi_A(1, 2)$	$1.711 * 10^{-14}$ F m ²
$\psi_A(2, 2)$	$1.613 * 10^{-12}$ F m ²
ρ_A	0.5
ρ_S	0.2
ρ_D	0.3
σ_C	$3.5 * 10^7$ S/m
$M_{3,3}$	333.12 Sm ⁴

Two simulations are run on the rigid plate, one including charging effects (electrostatic and

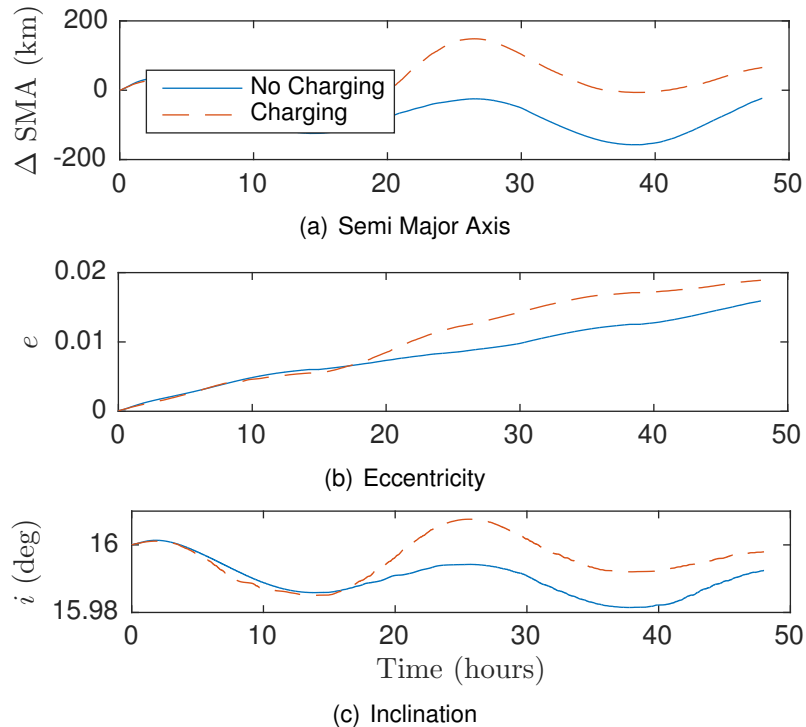


Figure 1.32: Change in classical orbital elements parameters due to charging

eddy currents) and one without. This is done to investigate the magnitude of the charging induced perturbations. The Lorentz field can only change the SMA by a few tens of meters per orbit, but electrostatic force and torque may couple to stronger perturbative forces to create large position differences after only a few orbits.

In this nominal case, the final positions of the plate after 48 hours of propagation with and without charging effects differ by 1474 km. When compared with the nominal SMA of 42,164 km, this difference appears small, however it corresponds to 2 degrees if projected in the velocity-normal plane. Also, over a longer integration period such as a week this difference could be much larger.

While it is interesting to look at the departure of the classical orbital elements, it is perhaps more applicable to look at collision risk. Uncontrolled debris, especially HAMR debris can drift far away from their nominal geostationary orbit. This case study considers an inclined orbit, which is not geostationary, but the drift can still be investigated.

The longitude and altitude departure from initial of both the charged and uncharged plate is shown in Fig. 1.33 for the 48 hour integration time. As one can see, both plates drift by more than 6 degrees in longitude, and nearly 1600 km in altitude. Both craft pass through geosynchronous altitude three times and could impact operational spacecraft at GEO.

Additionally, if these plates originated from defunct spacecraft in GEO graveyard orbit, typically between 200 and 300 km above geosynchronous, they could easily pass back through GEO and pose a collision risk.

This simulation was run again, but instead of keeping initial conditions the same and turning on charging, charging remained off for both runs but the initial attitude was changed from $\sigma = [0, 0, 0]^T$ to $\sigma = [0.1, 0, 0]^T$. This caused a final difference comparable to the distance caused by charging. This shows that propagation of HAMR objects is a very delicate and sensitive process, and electrostatic charging is one of the many things that need to be accounted for for very high

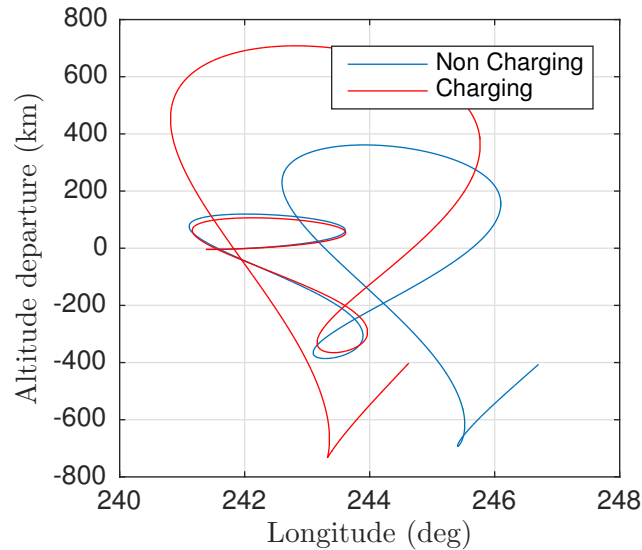


Figure 1.33: Longitude and altitude for plates with and without charging

fidelity propagation.

1.1.3.6.4 Trade studies

The single case of a 10 cm sheet showed reasonably significant differences caused by charging. To investigate the magnitude of charging effects on objects with different sizes and different initial conditions trade studies are performed. Running the two cases for 48 hours required 10 minutes of simulation time, in the following trade studies a simulation time of 12 hours is used for faster analysis.

1.1.3.6.4.1 Plate Area and Aspect Ratio

The first trade undertaken is one between the aspect ratio, total area, and the scalar difference between the final positions of the plate propagated with charging effects and the plate propagated without.

The area A is varied logarithmically from 1 cm² to 1 m², and the aspect ratio α is varied linearly from 1 to 10. The big and small sides denoted B and S are then given by

$$B = \sqrt{A\alpha} \quad S = B/\alpha \quad (1.118)$$

The offset between the center of mass and center of area is scaled to be 2% of corresponding side length:

$$\mathbf{r}_{\text{sep}} = [B/50, S/50, 0]^T \quad (1.119)$$

The results of this trade study are shown Figure 1.34. As one can see, the differences caused by charging are more noticeable when the the object is small, with the maximum displacement being 529 km which corresponds to 0.72° if projected perpendicular to radial. Even for objects large enough to track (10 cm²), differences over 100 km are not uncommon.

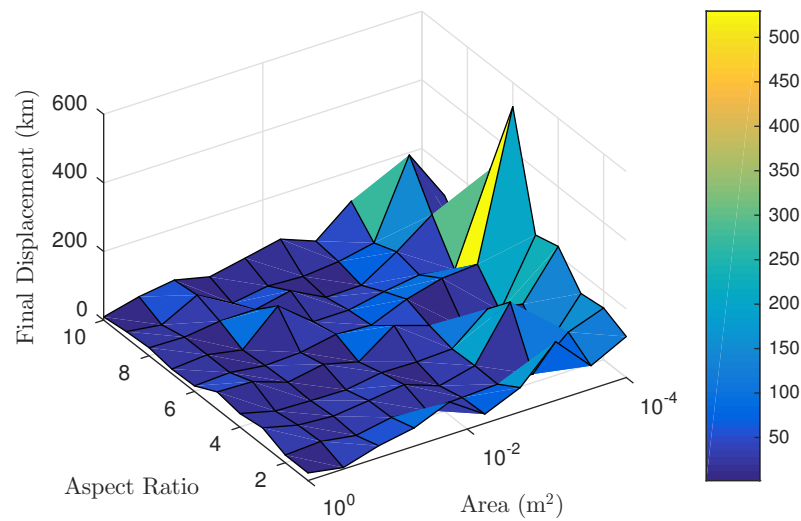


Figure 1.34: Differences in final state after 12 hours of propagating with and without charging effects

1.1.3.6.4.2 Initial attitude

The second trade study undertaken is in initial attitude. An initially sun pointing plate will have maximum SRP force and torque which will help it spin up faster. An initially anti sun pointing plate will have virtually no SRP force or torque until a separate perturbation such as electrostatics or gravity gradients change the attitude.

The dimensionless variable α is used to measure just how much the spacecraft is initially sun pointed. If the unit vector pointing to the sun is \hat{r}_s and \hat{k} is a random vector perpendicular to \hat{r}_s , we wish the body z axis to align with

$$\hat{z} = \alpha \hat{r}_s + (1 - \alpha) \hat{k} \quad (1.120)$$

The body x axis is found to be a separate random unit vector perpendicular to \hat{z} , and \hat{y} is found through $\hat{y} = \hat{z} \times \hat{x}$. A direction cosine matrix is formed from this set, and from that an initial MRP attitude is found.

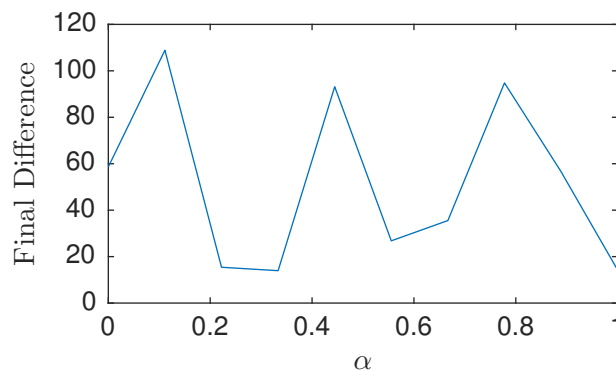


Figure 1.35: Difference in final positions as initial sun pointing angle changes

The difference in final positions with varying initial attitudes is shown in Fig. 1.35. There is not a strong trend in this trade study, but the variations caused by different initial attitudes vary greatly.

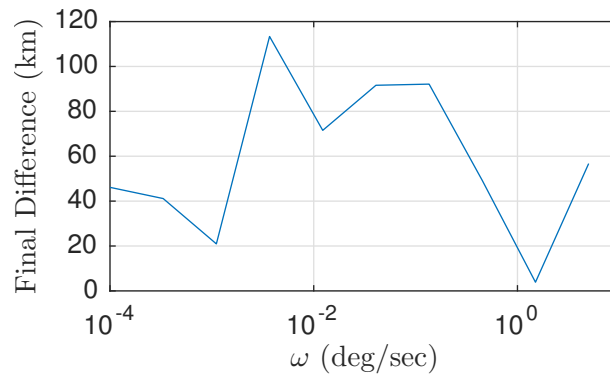


Figure 1.36: Difference in final positions as a function of initial spin rate

1.1.3.6.4.3 Initial Spin Rate

Many uncontrolled objects are tumbling due to external perturbative torques. If there is damping as there would be for a flexible structure, they may end up in a stable spin about their axis of major inertia. The third and final trade study is between the initial spin rate, which has been exactly zero in all previous simulations, and the distance between final states. The initial magnitude of the spin rate is varied logarithmically between $0.0001^\circ/\text{sec}$ and $5^\circ/\text{sec}$, and is given about the axis $[1, 2, 3]^T$. The results are shown on a semi-log plot in Figure 1.36. As one can see, there is not a strong trend in initial angular rate either. However, the differences caused by changing the initial rate are large—nearly 100 km in some cases.

1.1.3.6.5 Flat Field Analysis Summary

The effect of charging on perturbative propagation is investigated for HAMR objects. While the translational forces applied through charging are small and cannot move the debris very far per orbit, the electrostatic torques change the attitude which influences SRP which is capable of vastly changing the orbit. Oscillations of hundreds of kilometers are found with periods of a few days. Propagation is very sensitive to small differences either in charging or initial conditions. The only strong trend found was a clear increase in orbital changes for small objects.

Including charging is important for high fidelity propagation of HAMR orbits, especially if space weather has charged that object to very high voltages.

1.2 Research Thrust 2: Flexible Shape MSM Applications

One of the goals of the first year was to develop preliminary experiments in which flexible wires are deformed by Coulomb forces for comparison with to-be-developed flexible MSM models. The second and third year will investigate to what extent the MSM modeling can be expanding to flexible shapes which undergo deformations, as is the case with ripped off Mylar membranes. To develop a truth model, prototype experiments were proposed to compare against equivalent MSM models. The key challenge here is finding a suitable experiment that is simple enough to validate basic modeling capabilities of the MSM approach. Progress to date includes research into ideal sizes and types of wire, experimental setup of charged objects with a well-defined electric field, collection of necessary instruments, and code development for running these instruments. Each step provided various challenges detailed in the following sections.



Figure 1.37: 28AWG Wire Charged to 17.2kV and Exposed to $389\frac{kV}{m}$ Electric Field

1.2.1 Study Flexible Wire Shapes

The malleability exhibited by most conductors posed a significant challenge for developing a truth dataset. The hysteretic effects of compressive stresses on copper, which is usually delivered in a coil, complicates the testing procedure. The goal of studying wires prior to other shapes was predicated on the idea that all motion and forces would reside within a single plane — reducing the problem to two dimensions. However, most wires retain a helical structure when uncoiled. Multiple methods were considered for straightening the wire including heat treatment, application of high impulse tension forces, rolling the wire between two flat surfaces, and hanging the wire with a weight on the end for an extended period of time.

Coupled with this complication is the issue of flexibility. As shown in Figure 1.37, low-gauge copper wires resist Coulomb force deformation even when charged to kilovolts and exposed to large electric fields. This circumstance necessitated a different material or extremely thin copper wire. The latter option precluded some of the straightening methods discussed above but is preferred over the former which is neither convenient nor cost-effective. Applying a tension shock could break or work harden the thin wire while applying heat and/or a hanging mass were explored and discarded as ineffectual. However, rolling the wire between two flat surfaces proved effective. Calmont Ultraflex 36 AWG copper wire was selected due to its flexible, silicon-based sheath.

The alternative to using wire is a strip of mylar. Henceforth, the convention that length \gg width \gg thickness will be used such that a long, thin strip is described. Mylar is not malleable but is prone to creasing, which creates challenges similar to those posed by a wire. An additional complication is that, regardless of efforts to cut an extremely thin strip, the width of the cut is much greater than the thickness of the sheet. This geometric asymmetry pushes the experiment further from the ideal two dimensional situation, providing difficulties if the width is inconsistent along the length of the strip or if the electric field is not constant across the width of the strip. Either of these circumstances will inspire a twisting motion on the mylar strip.

1.2.2 Experiments on Wires

1.2.2.1 Atmospheric Experiments

The initial experiments were performed with a simple, constant electric field. A parallel-plate capacitor is the ideal geometry for this experiment. For a voltage $V_{pp} = V_+ - V_-$ applied to the



Figure 1.38: *Experimental Setup for Atmospheric Charge Deflection Experiments*

capacitor and a separation distance d , the electric field is well known

$$\mathbf{E} = \frac{V_{pp}}{d} \mathbf{e}_n \quad (1.121)$$

where \mathbf{e}_n is normal to the surface of the positive plate. This equation is most accurate near the center of two large, thin plates of side length s separated by a distance d such that $d \ll s$, minimizing edge effects.

As depicted in Figure 1.38, two aluminum plates are placed 2 inches apart. The positive and negative plates are connected to corresponding terminals on a Spellman CZE2000 high voltage power supply. Upstream of the power supply is a National Instruments DAQ which is connected to LabVIEW via USB. The LabVIEW virtual instrument provides a control interface for the power supply while also displaying the voltage and current on the plates.

Recalling the proper application of (1.121), a short wire was taped to hang near the center of the positive plate with the conductor of the wire in contact with the positive plate such that it is charged to

$$Q_{\text{wire}} = V_+ C_{\text{wire}} \quad (1.122)$$

The Coulomb force at a point y on the wire is then

$$\mathbf{F}_c(y) = \mathbf{E} Q_{\text{wire}}(y) = \frac{V_{pp}}{d} Q_{\text{wire}}(y) \mathbf{e}_n \quad (1.123)$$

This force as well as the weight force and the wire's resistance to bending are balanced with tension forces to satisfy Newton's 2nd law. The steady-state solution is one in which the torques sum to zero so that the wire is in equilibrium with its environment.

Figure 1.39(a) shows the experimental setup using a 2in length of the selected wire prior to charging. In these images, the background is a 0.25in grid which provides a way to determine deformation on the wire. Note that straightening methods were not utterly successful. The kink near the top of the wire persists throughout experiments, as seen in Figures 1.39(b) and 1.39(c).



(a) 36AWG Ultraflex Wire at 0V



(b) Plate and Wire Charged to 3kV



(c) Plate and Wire Charged to 5.2kV

Figure 1.39: *Charged Wire Experiments.*

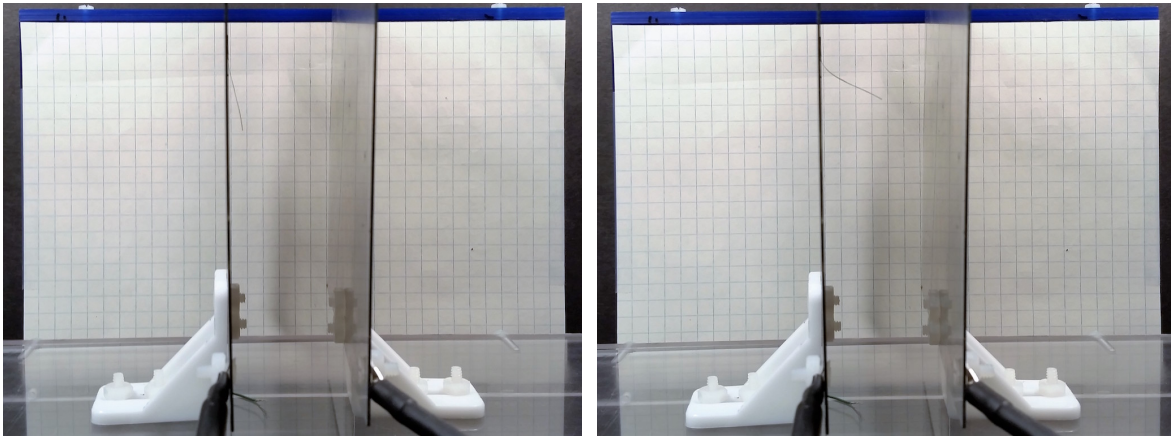
Experiments in which the wire and plate are charged to several kilovolts exhibit deformation, but not as expected. Some amount of curvature along the length of the wire was predicted in these experiments. However, Figure 1.39(c) shows the wire deformed into almost a perfect line. This behavior persists for a variety of voltages in between those shown here. In the near future, analyses will be run to determine whether this circumstance is an artifact of the experimental setup (i.e. the wire is too stiff) or is truly reflective of the system.

Experiments with the mylar strip provided results qualitatively similar to those of the wire. Due to the increased flexibility, the strip was cut to a shorter length (0.85in) to avoid the issue of arcing to the negative plate discussed in the next section. The mylar strip was roughly 0.06in wide — about 12 times larger than the diameter of the conductor of the wire — and 0.0015in thick. As discussed previously, this object is much closer to a sheet than a line. Experiments, however, showed no noticeable amount of twisting. This implies that the width of the strip is constant along its length and that the electric field is very nearly constant across the width of a strip.

Both Figures 1.39(b) and 1.39(c) show curvature of the mylar strip. An interesting result is that the sign of the curvature (concave up versus concave down) changes between the two trials. This could, again be an artifact of the experiment. Looking closely at Figure 1.40(a), the mylar strip exhibits a small amount of concave down curvature prior to charging. The deformation seen in Figure 1.40(b) could result from this circumstance.



(a) Mylar Strip at 0V



(b) Plate and Mylar Strip Charged to 3kV

(c) Plate and Mylar Strip Charged to 5.2kV

Figure 1.40: *Plate and Mylar Strip.*

A significant benefit of running identical experiments on two materials is the chance to compare results. Notice that Figure 1.40(c) shows curvature not seen in 1.39(c). This is because the tension forces between the two setups are different. The portion of mylar taped to the plate is identical to the remainder of the strip. The wire, on the other hand must have part of the shielding removed to make electrical contact with the plate. This offers two experimental setups — one in which only the conductor is taped to the plate and another where the conductor and some part of the shielding are taped down. The experiments discussed above use the former method because the latter generates a torque that deforms the wire, as shown in Figure 1.41. However, by taping only the conductor, a hinge is created at the point where the insulation starts. This is seen in Figure 1.39(c).

1.2.2.2 Vacuum Chamber

Vacuum chamber tests will proceed in a manner comparable to the atmospheric tests. The operative difference between the two environments will be electrical interaction with the air. At high enough voltages, air — which is usually an excellent insulator — begins to ionize and conduct electricity. This is undesirable because the resultant current through the wire changes the forces it experiences. Paschen's law describes the breakdown voltage for a gas as a function of the



Figure 1.41: Wire with Insulator Taped at 0V

separation distance l between two charged objects

$$V_B = \frac{Bpl}{\ln(Apl) - \ln[\ln(1 + \frac{1}{\gamma_{se}})]} \quad (1.124)$$

where p is atmospheric pressure — for this case — and A , B , and γ_{se} are physical constants of the gas. The variable l is used here because the distance between the two conductors need not be the same as the plate separation. Indeed, for these experiments $l < d$ because as the mylar or wire is deformed by Coulomb forces, the end moves closer to the negative plate. Figure 1.42 shows the breakdown voltage of air as a function of separation distance.

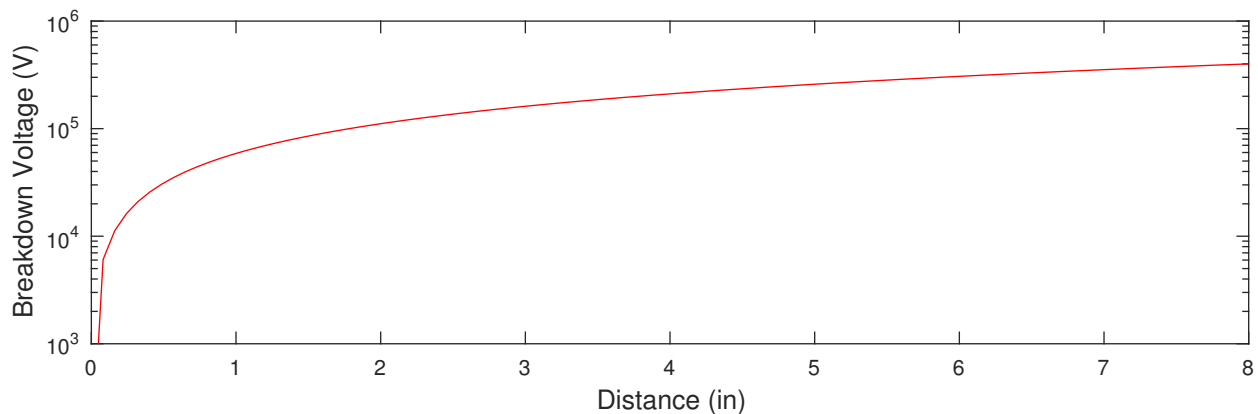


Figure 1.42: Breakdown Voltage of Air at Atmospheric Pressure

Revisiting Figure 1.40(c), it can be seen that $l \sim 0.5$ in. The graph above shows that this regime requires lower voltages to arc. Recall also that the more the voltage is increased, the smaller l becomes and the more the mylar or wire is deformed. It is desirable that the flexible conductor is long enough to clearly show deformation but also that the plates are close enough that edge effects are minimal, as discussed previously. These two situations motivate the use of a vacuum chamber. Experimental results²⁹ have shown that electrical breakdown voltages at pressures of $\sim 10^{-8}$ atm exceed 100kV over a 0.5in gap. This allows for the maximization of the mylar strip length, which will provide a larger data set.

1.2.3 Conclusions and Future Work

Considering the difficulties experienced throughout these experiments, the mylar strip appears the best choice for creating a truth dataset for MSM model comparison. Provided the mylar is not creased significantly and is cut carefully, the issues experienced when using a wire are mitigated.

While the current experimental setup provides a good dataset, an additional set which exhibits greater curvature across the mylar is desirable. This additional information would encourage more conclusive results on the MSM technique's ability to accurately model the deformation of charged, flexible conductors exposed to various electric fields. Future experiments will be conducted both with a flat field as described in the preceding sections and a curved field produced by means of a charged spherical shell. The electric field of such an object can be accurately modeled as the field from a point-charge

$$\mathbf{E} = -\frac{C_{\text{shell}}V_{\text{shell}}}{4\pi\epsilon_0 R^2}\mathbf{e}_r \quad (1.125)$$

where \mathbf{e}_r is the radial unit vector, $C_{\text{shell}}V_{\text{shell}}$ comes from the relationship to the total charge on the shell as described in Equation 1.122, and R is the magnitude of \mathbf{R} which points radially outward from the center of the spherical volume enclosed by the shell to the point at which the electric field is calculated.

An additional improvement on the current setup would include a different method of holding the mylar strip and a different voltage on the strip than on the plates/sphere. Both of these goals can be accomplished by the use of a conducting clamp attached to a different high voltage power supply than that being used to charge the plate/sphere. With these changes, the effects of taping the strip are further mitigated and many more trials can be conducted.

1.3 Research Thrust 3: Dielectric Surfaces

Determining the force and torque on a charged conducting spacecraft is a complex task. Spacecraft with some dielectric surfaces add many challenges. Firstly, there are now multiple voltages to solve for rather than just the frame voltage. Depending on the geometric complexity of the spacecraft, this can require tens to hundreds of variables. The voltage and charge on each facet will influence the current collected by all other facets. Additionally, the charging timescale for dielectrics is much larger than for a pure conductor. This means that rather than assuming that the spacecraft is always at equilibrium with its surroundings and root solving the current balance, the differential equations must be integrated.

1.3.1 Study Time Dependent Dielectric Charging

A completely conducting spacecraft will typically have will typically have a capacitance to space of a few hundred picoFarads. Environmental currents are typically a few tens of microAmps. This leads to charging times of a few milliseconds. However, if dielectrics are present, there are capacitances between different parts of the spacecraft. These capacitances are typically much larger, for instance a 1 mil thick square of mylar 1 m to an edge has a capacitance to the spacecraft frame of a few μ Farads. This dielectric will have a charging time of a few tens of seconds. High energy particles (MeV) can burrow deep into dielectrics and change the incident currents by creating potential wells. These effects combine to create a complex multi-dimensional problem with a timescale of hours.

An added complexity when moving to dielectrics rather than conductors is that the spacecraft may be at many different voltages at once. Rather than just solving for one variable, which only a function of time because environmental parameters change, one must solve for a coupled set of variables which have direct temporal dependence. An added effect of dielectrics is polarization. Although this polarization needs to be considered for high-fidelity charging and especially for discharge events, the electrons are only moving from the effective center of the atom to the edge. This displacement is less than an angstrom which is much smaller than the displacements that occur in conductors where charge can flow freely. Of course, this polarization may lead to arcing, during which the charge distribution may change dramatically, but modeling arcing is beyond the scope of this project. The changes to the charge distribution are more dramatic with conductors – for example in typical ambient Lorentz fields, $v \times B \approx 0.1$ mV/m the center of charge can be displaced by a micron, and for large inter-craft fields (\sim kV/m) as are seen in the Electrostatic Tractor, the displacement can be more than a meter. For the purposes of computing electrostatic force and torque, polarization can be neglected.

To solve for the voltage and charge distribution of a spacecraft that is not entirely conducting, a simulation has been written. The state of this simulation is the charge of each facet of the spacecraft. For instance, a spacecraft with two solar panels with isolated coverglasses might have three facets: the frame and each solar panel. At each timestep, the currents to and from each facet are computed in order to change the charge and voltage. The environmental currents are all functions of their voltage and illumination, although in reality potential wells caused by nearby charging can affect this. The currents between facets must also be computed. The currents between conducting facets act to instantaneously remove any voltage difference across them. The currents to each node are given by

$$\mathbf{I} = \frac{\mathbf{q}_c - \mathbf{q}}{dt} \quad (1.126)$$

Where \mathbf{q}_c a vector containing the charge each facet should have, \mathbf{q} is a vector containing the actual charge, and dt is the time step. To find how much charge each facet should have, the total voltage must be computed

$$V = \frac{\sum [C_c] \mathbf{V}_c}{\sum \sum [C_c]} \quad (1.127)$$

Where $[C_c]$ is a subset of the total capacitance matrix containing only the conducting facets, \mathbf{V}_c is a vector of the voltages of each conducting facet, and V is the scalar voltage of the conductor. Once the scalar voltage is known, the desired charge to remove voltage differences can be computed.

$$\mathbf{q}_c = [C_c] \mathbf{1} V \quad (1.128)$$

Where $\mathbf{1}$ is a column vector of ones the appropriate size. The currents between two facets that are not both conducting could be calculated using Ohms Law:

$$I = \frac{\Delta V}{R} \quad (1.129)$$

Where R is the resistance between the two facets. Quantifying the importance of the leakage current for force and torque calculations is a challenge for future work. At present leakage currents are not included.

Because not all the facets are sunlit, and many may have different SEY properties, and the voltage of each facet depends on the charge stored on all other facets, such simulations are quite complex. Additionally, since there are many different timescales (the frame will have a time scale

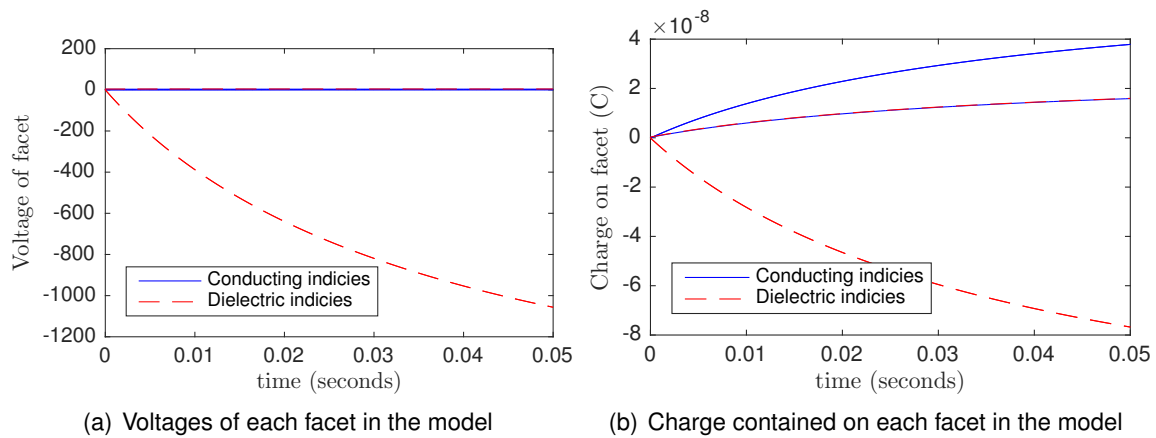


Figure 1.43: Voltage and charge on each facet in a model.

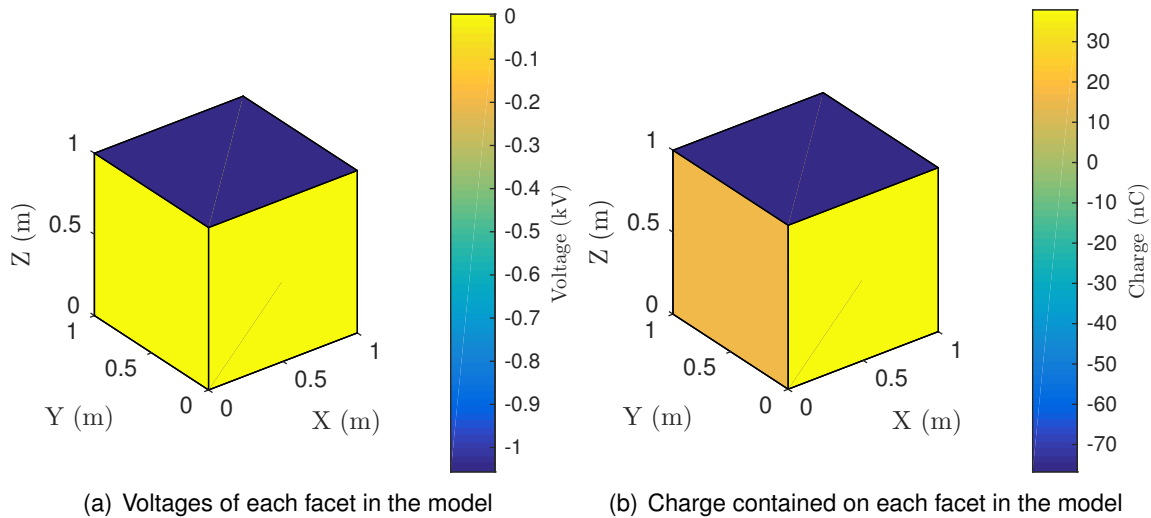


Figure 1.44: Final state in voltage and charge for the cube

of ms, while the dielectrics may have a time scale of hours), the simulations can take a long time to run.

As an example, consider a 1 meter cube with three sides aluminum, 3 sides made from unsupported kapton, and 2 sides (one of each material) sunlit. The fact that the kapton is unsupported means that it is not on top of the frame, rather it is suspended like the skin of a drum. This means that the kapton does not have a high capacitance to the spacecraft frame, and consequently the charging times are short.

As one can see, the conducting facets all have the same voltage, although they have different amounts of charge. The dielectric facets, shown as dashed lines, are all over the place in voltage and charge. The final state in charge and voltage is shown on the physical model below. The two yellow faces in the voltage plot are sunlit, and as expected they are very close to 0 V. The top face (dark blue in both voltage and charge) is dielectric and shaded. This allows it to charge to more than a kilovolt. Because the two sunlit faces are different materials, they have different SEE parameters and charge to different but close voltages. Because of the adjacent dielectric, the difference in charge is more dramatic.

1.3.2 Consider space dielectric charging (Nascap-2K)

There are many programs to model the charging of complex spacecraft in realistic space environments. The state of the art is the Nasa Spacecraft Charging Analysis Program (NASCAP). The most current iteration of this program is Nascap 2k which has many added capabilities. Nascap allows simulation of spacecraft in GEO, LEO, and polar orbiting spacecraft in varying space weather conditions. A screen capture of the voltages on a template GEO spacecraft is shown below:

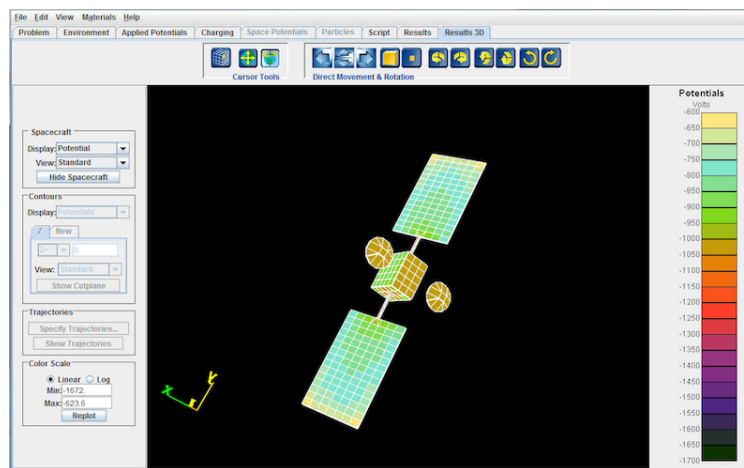


Figure 1.45: Example Nascap simulation

Nascap is free and open source, but only available to US citizens. Our lab has acquired a copy and installed the program on our export controlled server. It is currently being used to produce truth models for the charging of complex non-conducting spacecraft. These can validate or supplement the dielectric charging simulations created previously. If the capacitance matrix can be exported, the charge on each facet can be computed and a simple program can be written to compute forces and torques. Which can be used to fit MSM models to non-conducting spacecraft. If the capacitance matrix cannot be exported, Nascap will be used to compute the voltages, and a similar model will be created to translate the voltages to charges, and eventually to force and torque.

The Nascap software has been obtained and installed on an export-controlled computer. While the general output of Nascap is not export-controlled, the software itself is only available to U.S. citizens. Thus, the lab established an export control plan with the University of Colorado to create a protected means to use and access this software in the next project year.

1.3.3 Expand MSM model to incorporate insulators

Many challenges exist when including dielectrics into the existing MSM framework. Currently MSM uses a small number of spheres that can be placed anywhere within the body to estimate force and torque. If dielectrics are present, there may be constraints needed on the positions of some spheres. Furthermore, to adequately represent the condition of a charged insulator on top of an oppositely charged conducting spacecraft frame, large spheres that are nearly overlapping may be required.

For some shapes, having spheres with separations smaller than their radii has made the matrix singular or badly conditioned. Inverting the inverse capacitance matrix has proved difficult in the past, as the determinant can become close to zero for certain sphere position and sizes. Further

work is required to quantify the significance of differently charged dielectrics for computing force and torque, and how best to modify MSM to model them if needed.

During the second project year theories will be developed on how to efficiently integrate insulators into the MSM modeling. The first year allowed us to begin studying the modeling of di-electric charging, which continues into the second year. We have also developed rough augmented MSM model ideas, but these are too early to report details or modeling performance on. Overall this last task has just started and is ramping up for an in-depth investigation.

Chapter 2

Conclusions and Planned Work

2.1 Conclusions

The first project year was very fruitful with several key advances being made in the faster-than-realtime modeling of spacecraft electrostatic forces and torques. In particular, the Volume Multi-Sphere-Method (VMSM) setup process has undergone significant revisions and enhancements, and the latest results look very promising in approximating the complex E-field with a small number of optimally placed spheres. Studying the new Appropriate Fidelity Measures (AFMs) has provided insight into the complex expansion of E-fields about general bodies, and also provides the self-capacitance constraint which allows us to do the numerical MSM fitting. This work has been published in 2 conference papers, and related journal papers are in preparation.

Work has also progressed on doing atmospheric electrostatic deflection experiments to study the electrostatic forces during small shape changes. The thin Au-coated mylar strips provide the most promising results thus far.

Modeling di-electrics using MSM methods is progressing well. Augmented MSM models are being considered that account for the limited charge motion of di-electrics, and their ability to accumulate charge from the environment.

The project is on-time and on-cost. The reduced first year budget was accounted for in the spending, and we are increasing the graduate student support in the fall to account for the shifted year 2 funds. We are very excited with the range and quality of the results obtained thus far, and looking forward to 2nd year.

2.2 Year 2 Planned Work

The second year research efforts will proceed mostly as planned, with the inclusion of the AFM models in the analysis. The MSM fitting on conducting rigid body shapes will be mostly done by the 2nd year, leaving only smaller documentation follow-up work for year 3. A key new focus of project year 2 is the inclusion of atmospheric and vacuum chamber based electrostatic actuation test. Also, expanding on the MSM theory to account for di-electric surfaces presents a good research challenge. We have staffed the project with all required graduate research assistant who are eager and well-qualified to pursue this research.

Bibliography

- [1] Gibson, W. C., *The method of moments in electromagnetics*, Chapman & Hall, November 28 2007.
- [2] Brebbia, C. A., *The Boundary Element Method for Engineers*, Pentech Press, 1978.
- [3] Stevenson, D. and Schaub, H., “Multi-Sphere Method for Modeling Electrostatic Forces and Torques,” *Advances in Space Research*, Vol. 51, No. 1, Jan. 2013, pp. 10–20, doi:10.1016/j.asr.2012.08.014.
- [4] Schaub, H. and Sternovsky, Z., “Active Space Debris Charging for Contactless Electrostatic Disposal Maneuvers,” *Advances in Space Research*, Vol. 43, No. 1, 2014, pp. 110–118, doi:10.1016/j.asr.2013.10.003.
- [5] Lai, S. T., *Fundamentals of Spacecraft Charging: Spacecraft Interactions with Space Plasmas*, Princeton University Press, 2011.
- [6] Stevenson, D. and Schaub, H., “Optimization of Sphere Population for Electrostatic Multi Sphere Model,” *IEEE Transactions on Plasma Science*, Vol. 41, No. 12, Dec. 2013, pp. 3526–3535, doi:10.1109/TPS.2013.2283716.
- [7] Jasper, L. E. Z. and Schaub, H., “Effective Sphere Modeling for Electrostatic Forces on a Three-Dimensional Spacecraft Shape,” *Adventures on the Interface of Dynamics and Control*, edited by K. T. Alfriend, M. Akella, J. E. Hurtado, J. Juang, and J. D. Turner, Tech Science Press, Duluth, Georgia, 2012, pp. 267–298.
- [8] Bauer, R., “Distriubtion of POints on a SPHERE with Applicaiton to Star Catalogs,” *AIAA Journal of Guidance, Control, and Dynamics*, Vol. 23, No. 1, 2000, pp. 130–137, doi:10.2514/2.4497.
- [9] Hughes, J. and Schaub, H., “Appropriate Fidelity Electrostatic Force Evaluation Considering a Range of Spacecraft Separations,” *AAS/AIAA Spaceflight Mechanics Meeting*, Napa Valley, California, Feb. 14–18 2016, Paper No. AAS-16-486.
- [10] Griffiths, D. J., *Introduction to Electrodynamics*, Prentice Hall, 3rd ed., 1999.
- [11] Schaub, H. and Junkins, J. L., *Analytical Mechanics of Space Systems*, AIAA Education Series, Reston, VA, 3rd ed., 2014, doi:10.2514/4.102400.
- [12] Giancoli, D. C., *Physics for Scientists and Engineers*, Pearson Prentice Hall, 2008.
- [13] Hughes, J. and Schaub, H., “Rapid Electromagnetic Force and Torque Evaluation for Geometrically Complex Spacecraft,” *Advanced Maui Optical and Space Surveillance Technologies Conference*, Maui, Hawaii, Sept. 26–30 2016.

- [14] Schildknecht, T., Muscia, R., Plonera, M., Beutlera, G., Fluryb, W., Kuuselac, J., de Leon Cruzd, J., and de Fatima Dominguez Palmerod, L., "Optical observations of space debris in GEO and in highly-eccentric orbits," *Advances in Space Research*, 2004, pp. 901–911.
- [15] Wiesel, W. E., "Estimating Nongravitational Accelerations on High Area-to-Mass Ratio Objects," *AIAA Journal of Guidance, Control, and Dynamics*, Vol. 39, No. 6, 2016, pp. 1438–1443, doi:10.2514/1.G001464.
- [16] Früh, C., Ferguson, D., Lin, C., and Jah, M., "The Effect of Passive Electrostatic Charging on Near-Geosynchronous High Area-To-Mass Ratio Objects," *International Astronautical Congress*, Vol. 64, 2013.
- [17] Schildknecht, T., Musci, R., Frueh, C., and Ploner, M., "Color Photometry and Light Curve Observations of Space Debris in GEO," *Proceedings of the Internaitonal Astronautical Congress*, 2008.
- [18] Dever, J. A., de Groh, K. K., Townsend, J. A., and Townsend, J. A., *Mechanical Properties Degradation of Teflon FEP returned from the Hubble Space Telescope*, American Institute of Aeronautics and Astronautics, 1998.
- [19] Fennell, J. F., Koons, H. C., Leung, M., and Mizera, P., "A review of SCATHA satellite results: Charging and discharging," Tech. report, Space Division Air Force Systems Command, Los Angeles Air Force Station, Aug. 1985.
- [20] Gómez, N. O. and Walker, S. J., "Eddy currents applied to de-tumbling of space debris: Analysis and validation of approximate proposed methods," *Acta Astronautica*, Vol. 114, 2015, pp. 34–53, doi:10.1016/j.actaastro.2015.04.012.
- [21] Anderson, P. V. and Schaub, H., "Local Orbital Debris Flux Study in the Geostationary Ring," *Advances in Space Research*, Vol. 51, No. 12, 2013, pp. 2195–2206, doi:10.1016/j.asr.2013.01.019.
- [22] Wie, B., *Space Vehicle Dynamics and Control*, AIAA Education Series, Reston, VA, 2nd ed., 2008.
- [23] Maxwell, J., *A Treatise on Electricity and Magnetism*, Oxford University Press, 1893.
- [24] Allen, D. N. D. G. and Dennis, S. C. R., "The Application of Relaxation Methods to the Solution of Differential Equations in Three Dimensions," *Quarterly Journal of Mechanics and Applied Mathematics*, Vol. 6, 1953, pp. 87.
- [25] Reitan, D. K. and Higgins, T. J., "Accurate Determination of the Accurate Determination of the Capacitance of a Thin Rectangular Plate," *Transactions of the American Institute of Electrical Engineers, Part I: Communication and Electronics*, Vol. 75, No. 6, 1957, pp. 761–766.
- [26] Tsyganenko, N. A., "A Magnetospheric magnetic field model with a warped tail current sheet," *Planetary and Space Science*, Vol. 37, 1989, pp. 5–20.
- [27] Früh, C., Ferguson, D. C., Lin, C., and Jah, M. K., "The effect of passive electrostatic charging on near-geosynchronous high area to mass ratio objects," *64th International Astronautical Congress*, Sept. 23–27 2013, Paper No. IAC-13-A6.2.8.

-
- [28] McMahon, J. and Scheeres, D. J., "A New Navigation Force Model for Solar Radiation Pressure," *AIAA Journal of Guidance, Control and Dynamics*, Vol. 33, No. 5, 2010, pp. 1418–1428.
- [29] Mulcahy, M. and Bolin, P., "High Voltage Breakdown Study," Tech. report, United States Army Electronics Command, 1971.